Title: Molecular basis of mitotic decline during human aging

Authors: Joana Catarina Macedo[1,2], Sara Vaz[1,2], Bjorn Bakker[4], Rui Ribeiro[1,2], Petra Bakker[4], Jose Miguel Escandell[5], Miguel Godinho Ferreira[5], René Medema[6], Floris Foijer[4] and Elsa Logarinho[1,2,3]*

Affiliations:

[1] Aging and Aneuploidy Laboratory, IBMC, Instituto de Biologia Molecular e Celular, Universidade do Porto, 4200-135 Porto, Portugal.

[2] i3S, Instituto de Investigação e Inovação em Saúde, Universidade do Porto, 4200-135 Porto, Portugal.

[3] Cell Division Unit, Department of Experimental Biology, Faculty of Medicine, Universidade do Porto, 4200-319 Porto, Portugal.

[4] European Research Institute for the Biology of Aging, University of Groningen, University Medical Center Groningen, NL-9713 AV Groningen, The Netherlands.

[5] Instituto Gulbenkian de Ciência, Oeiras, Portugal.

[6] Division of Cell Biology I, The Netherlands Cancer Institute, The Netherlands.

*Corresponding author/lead contact: email: elsa.logarinho@ibmc.up.pt; phone: +351 220 408 800.

Abstract: Aneuploidy, an abnormal chromosome number, has been linked to aging and age-associated diseases, but the underlying molecular mechanisms remain unknown. Supported by direct live-cell imaging of young, middle-aged and old-aged primary human dermal fibroblasts, we found that aneuploidy increases with aging due to general dysfunction of the mitotic machinery. Increased chromosome segregation defects in elderly mitotic cells correlated with an early senescence-associated secretory phenotype (SASP) and repression of Forkhead box M1 (FoxM1), the transcription factor that drives expression of most G2/M genes. By restoring FoxM1 levels in elderly and Hutchison-Gilford Progeria Syndrome fibroblasts we prevented aneuploidy and, importantly, ameliorated cellular phenotypes associated with aging. Moreover, senescent fibroblasts isolated from elderly donors' cultures were mostly aneuploid, suggesting that aneuploidy is a key player in the progression into full senescence phenotypes. Based on this feedback loop between cellular aging and aneuploidy, we propose modulation of mitotic efficiency through FoxM1 as a potential strategy against aging and progeria syndromes.

Aging has been linked to an increase in aneuploidy for the past several decades [1]. This association has been well documented for oocytes and is considered to be the main cause of miscarriage and birth defects in humans [2]. However, aneuploidy can also arise in somatic cells, and a number of studies have reported age-dependent increases in aneuploidy [3–7]. These studies have shown that aging is positively correlated with the incidence of chromosome mis-segregation, raising the question whether there is a general dysfunction of the mitotic apparatus in aged cells [8]. Transcriptome analyses of a panel of fibroblast and lymphocyte cultures from young and old individuals revealed changes in the expression of genes controlling the mitotic machinery [9,10]. However, the use of mixed cell populations in different stages of the cell cycle

and the lower mitotic indexes of elderly cell cultures has limited these studies from clearly demonstrating whether mitotic genes are repressed intrinsically in old dividing cells. Moreover, analysis of the mitotic process in aging models and diseases has been scarce and a comprehensive analysis of cell division efficiency in naturally aged cells is largely missing.

More recently, aneuploidy has been also linked to aging. Studies of aneuploidy-prone mouse models exhibiting increased rates of chromosome mis-segregation uncovered a unanticipated nexus with the rate of aging and the development of age-related pathologies [11–14]. Mutant mice with low levels of the spindle assembly checkpoint protein BubR1 were found to develop progressive aneuploidy along with a variety of progeroid features, including short lifespan, growth retardation, sarcopenia, cataracts, loss of subcutaneous fat and impaired wound healing [11]. In addition, systematic analyses of disomic yeast, trisomic mouse and human cells, all cells with an extra chromosome, have elucidated the impact of aneuploidy in cellular fitness [15]. The cumulative effect of copy number changes of many genes induces the so called pan-aneuploidy phenotypes [16], namely proliferation defects [17,18], gene signature of environmental stress response [19,20], multiple forms of genomic instability [21–23], and proteotoxicity [24–26], which interestingly, are cellular hallmarks of aging [27].

Together, these observations suggest that there is a positive correlation between aging and aneuploidy but evidence for mitotic decline in elderly dividing cells and for aneuploidy-driven permanent loss of proliferation capacity (full senescence) is limited. Here, we used live cell time-lapse imaging to investigate the mitotic behavior of human dermal fibroblasts collected from healthy Caucasian males with ages ranging from neonatal to octogenarian and cultured under low passage number. We show mitotic duration to increase with advancing age alongside with a higher rate of mitotic defects. We demonstrate this mitotic decline to arise from a transcriptional

shutdown of mitotic genes in pre-senescent dividing cells exhibiting senescence-associated secretory phenotype (SASP). We show short-term induction of FoxM1 transcriptional activity to improve mitotic fitness and ameliorate senescence phenotypes in elderly and progeroid cells. Finally, we identify aneuploidy as a major hallmark of full senescence in naturally aged cells thus pointing up for the potential of mitotic fitness enhancement as an anti-aging strategy.

Results

Aneuploidy increases during natural aging

In our study we used human dermal fibroblasts (HDFs) collected from healthy Caucasian males with ages ranging from neonatal to octogenarian (Supplementary Fig.1a), to test whether aneuploidy increases during natural aging and if this is a consequence of a general dysfunction of the mitotic machinery in aged cells. Since inter-individual differences exist in the rate at which a person ages (biological age), we included two donors of each age in a total of five chronological ages to increase the robustness of any correlation found with chronological aging. In addition, we used dermal fibroblasts from an 8 years-old child with the Hutchison-Gilford progeria syndrome (HGPS) as a model of premature cellular aging [28]. Considering that during a normal post-natal lifespan cells *in vivo* will hardly reach the exhaustion number of replications observed in culture [29], and to limit any artifacts and clonal selection of *in vitro* culturing, only early cell culture passages way below replicative lifespan exhaustion were used (Population doubling level (PDL)<24). Chronic accumulation of macromolecular damage during natural aging induces a cellular stress response known as senescence [30], and accumulation of senescent cells has been widely used to reflect biological age and linked to pathological aging [31,32]. Accordingly, we found significantly higher levels of senescence-associated (SA) biomarkers [33], measured under

89 strict quantitative parameters by microscopy analysis, in the proliferating fibroblast cultures from
90 older individuals and the HGPS patient (Supplementary Fig.1b-g), thus validating their
91 suitability as models of advanced and premature aging, respectively.

92 To determine if aneuploidy increases with aging, we performed fluorescence *in situ*
93 hybridization (FISH) analysis for three chromosome pairs. We found significantly higher
94 aneusomy indexes in asynchronous cell populations of middle-aged, old-aged and progeria
95 samples (Fig. 1a,b). However, because aneuploid cells are most likely outcompeted in culture by
96 diploid cells [17], thereby diluting the aneuploidy index, we additionally measured aneuploidy in a
97 post-mitotic cell subpopulation generated during a 24h treatment with the cytokinesis inhibitor
98 cytochalasin D (Fig. 1a,c). Using this approach, we observed even higher aneuploidy in the
99 middle-aged, old-aged and progeria cultures. Thus, the mild aneuploidy levels found in elder
100 cultures support the idea of an age-associated loss of mitotic fidelity.

101 *Elder cells divide slower with increased rate of mitotic defects*

102 To gain insight into how old cells divide, we followed individual mitotic cells by long-term
103 phase-contrast time-lapse imaging. Interestingly, we found the interval between nuclear envelope
104 breakdown (NEB) and anaphase onset to increase steadily with advancing age (Fig. 1d-e). To
105 exclude any effects due to genetic heterogeneity between the Caucasian donors and to
106 discrepancies in culture population doubling levels, we used mouse adult fibroblasts recurrently
107 sampled from female mice over a period of 2 years. In this model, culture conditions were highly
108 controlled, thereby providing a solid "ex vivo" model of chronological aging. Again, both
109 mitotic duration (Supplementary Fig.2a-c) and senescence-associated biomarkers
110 (Supplementary Fig.2d-e) progressively increased with aging.

111 We then asked what could be leading to the age-associated mitotic delay. Bypass of short

112 telomere-triggered senescence by disruption of tumor-suppressive pathways, shown to elicit
113 telomere fusion-driven prolonged mitosis [34], was ruled out as potential cause since we found no
114 evidence for chromosome fusions in metaphase spreads of the primary dermal fibroblasts used in
115 our study (Supplementary Fig.3a). Activation of the spindle assembly checkpoint (SAC) by
116 defective kinetochore-microtubule attachments and/or reduced efficiency of the ubiquitin-
117 proteasome system induced by proteotoxic stress could alternatively explain the delay between
118 NEB and anaphase onset in older cells. We found the mitotic delay to depend on SAC activity as
119 treatment with a small molecule inhibitor of the Mps1 kinase rescued mitotic duration to similar
120 levels in all cell cultures (Fig. 1d,f). Enhancement of proteasome activity with a small molecule
121 inhibitor of the Usp14 deubiquitinase did not change mitotic duration considerably
122 (Supplementary Fig.3b). As a correlation between cell size, mitotic duration and SAC strength
123 was recently described [35], we further tested whether aging-associated mitotic delay was due to
124 increased cell size. We found no significant correlation between mitotic duration and cell size in
125 fibroblast cultures (Supplementary Fig.3c-f). In addition, when treated with the kinesin-5
126 inhibitor (STLC) to induce chronic activation of the SAC, elderly cells arrested in mitosis as long
127 as young cells before they slipped out, suggesting SAC strength is similar (Supplementary
128 Fig.3g).

129 To investigate chromosome and/or spindle defects contributing to increased mitotic duration in
130 older cells, we performed high-resolution spinning-disk confocal microscopy in cells expressing
131 H2B-GFP and α-Tubulin-mCherry. We found several mitotic defects to be significantly
132 increased in middle-aged and old-aged samples (Fig. 2a-d), namely chromosome congression
133 delay (Fig. 2b), anaphase lagging chromosomes (Fig. 2c) and spindle mispositioning in relation
134 to the growth surface (Fig. 2d). These phenotypes were quantified by scoring the percentage of

cells exhibiting severe vs. mild chromosome mis-segregation following treatment with the Mps1 inhibitor (Fig. 2e; Supplementary Fig.4a); micronuclei [36] (Fig. 2f); spindle mispositioning (Fig. 2g, Supplementary Fig.4b-d); and cytokinesis failure (Fig. 2h). Overall, the data indicated that alongside increased aneuploidy, aging triggers abnormalities at several mitotic stages.

Elderly mitotic fibroblasts exhibit SASP and transcriptional shutdown of mitotic genes

To identify the molecular mechanisms behind this complex aging-associated mitotic phenotype, we performed RNA sequencing (RNA-seq) gene expression profiling of cells captured in mitosis accordingly to the experimental layout shown in Fig. 3a. This procedure yielded purified cell populations with mitotic indices >95% in both neonatal and 87y donor cultures (Fig. 3b). RNA-seq revealed that the abundance of 3,319 gene transcripts was significantly altered in octogenarian mitotic fibroblasts compared to neonatal mitotic fibroblasts (Fig. 3c). Principal component analysis (PCA) showed that the biological replicates were consistent (Fig. 3d). In agreement with the elderly cell defects in mitosis, the top 10 most altered Gene Ontology (GO) terms included 7 cell cycle- and mitosis-related gene ontologies (Fig. 3e). 105 'mitotic cell cycle' genes were significantly altered in octogenarian mitotic fibroblasts (p-value<0.05; Supplementary Table 1), representing a 1.7-fold enrichment of alterations in this gene set (p-value=8.4E-9) (Fig. 3g). Moreover, we found significantly altered expression of 16 out of 29 cytokines, metalloproteinases (MMPs) and other factors previously associated with the senescence-associated secretory phenotype (SASP) [37], in the elderly vs. neonatal mitotic cells (Fig. 3f). Thus, an unforeseen SASP phenotype evolves in elderly dividing cells, alongside a global transcriptional shutdown of mitotic genes, likely accounting for aging-associated mild aneuploidy levels.

FoxM1 repression dictates mitotic decline during natural aging

158 RNA-seq analysis also disclosed Forkhead box M1 (FOXM1), the transcription factor that
159 primarily drives the expression of G2/M cell cycle genes, to be downregulated in elderly mitotic
160 cells (logFC:-0.85; FDR<5%; Supplementary Table 1). Indeed, 66 out of the 105 'mitotic cell
161 cycle' genes altered in the octogenarian fibroblasts have been reported as targets of the Myb-
162 MuvB (MMB)-FOXM1 transcription complex containing the cell cycle genes homology region
163 (CHR) motif in their promoters [38,39] (Supplementary Fig.6a). In addition, loss of FOXM1 has
164 previously been shown to cause pleiotropic cell-cycle defects leading to embryonic lethality [40].
165 We therefore asked whether loss of mitotic proficiency during normative aging was due to
166 FOXM1 downregulation. Indeed, increasing age correlated with decreased FoxM1 transcript and
167 protein levels in our human (Fig. 4a-c) and mouse (Supplementary Fig.2f) samples. Importantly,
168 unlike previous studies linking FoxM1 repression and aging [41,42], by analyzing the
169 transcriptomes of mitotic cells only, we uncoupled FoxM1 downregulation from the subsequent
170 reduction in cell proliferation, demonstrating that elderly cells divide with intrinsically low levels
171 of FoxM1. We thus conclude that aging-associated FoxM1 repression likely accounts for the
172 transcriptional shutdown of mitotic genes and the observed phenotypes in pre-senescent dividing
173 cells.

174 To test the correlation between FoxM1 repression and age-associated phenotypes further, we
175 RNAi-depleted FoxM1 in fibroblasts from the 10 years-old donor (Supplementary Fig.5a,b) and
176 performed RNA sequencing (RNA-seq) gene expression profiling of cells captured in mitosis.
177 RNA-seq revealed that FoxM1 repression significantly altered the abundance of 4,451 gene
178 transcripts (Supplementary Fig.6b,c; Supplementary Table 1), which were enriched for 'mitotic
179 cell cycle' genes (206 genes, Gene Ontology [GO] analysis; 5% FDR) (Fig. 4d). This constituted
180 a 2.52-fold enrichment of alterations in this gene set (*p*-value=1.09E-42). The top ten most

altered GO terms included five related to mitosis (Supplementary Fig.6e), and 217 out of 249 G2/M cell cycle genes previously reported as targets of the DREAM (DP, RB-like, E2F4 and MuvB) and MMB-FOXM1 transcriptional complexes [43], were downregulated following FoxM1 depletion (Supplementary Fig.6e). In agreement with these transcriptional alterations, FoxM1-depleted young fibroblasts displayed a mitotic delay (Fig. 4e), mitotic defects (Supplementary Fig.5c-e) and increased aneuploidy (Fig. 4f,g) similarly to old-aged fibroblasts. Interestingly, the percentage of cells with SA biomarkers (Fig. 4h,i), as well as the expression of SASP genes itself (Fig. 4j) also increased following FoxM1 repression. Altogether, these results show that young cells with low levels of FoxM1 recapitulate the aging-associated mitotic defects, aneuploidy and senescence.

Constitutively active FoxM1 rescues mitotic decline and cellular senescence in elderly and HGPS cells

As FoxM1 depletion reduced mitotic fidelity and induced senescence in young cells, we hypothesized that FoxM1 overexpression in elderly cells should counteract aging phenotypes. Expression of a constitutively active truncated form of FoxM1 (FoxM1-dNdK) in old-aged fibroblasts [44,45] (Supplementary Fig.5f,g) resulted in altered expression of 1,955 gene transcripts as determined by RNA-seq (Supplementary Fig.6b,d; Supplementary Table 1), including 85 'mitotic cell cycle' genes (Fig. 5a). Moreover, 149 out of the 249 DREAM/MMB-FOXM1 gene targets were significantly upregulated following FoxM1-dNdK expression (Supplementary Fig.6e). In addition, we found extensive overlap between genes of mitosis-related GO terms that were downregulated in FoxM1 RNAi and upregulated in FoxM1-dNdK expression experiments (1,163 genes; Supplementary Fig.6e; Supplementary Table 2). Concordantly, the age-associated mitotic defects were ameliorated in elderly fibroblasts expressing FoxM1-dNdK (Fig. 5b,c;

Supplementary Fig.5h-j), resulting in decreased aneuploidy levels (Fig. 5d,e). Furthermore, the percentage of cells with SA biomarkers (Fig. 5f,g) and the transcript levels of SASP genes (Fig. 5h) were decreased. Importantly, FoxM1-dNdK expression also partly rescued the mitotic defects, aneuploidy levels and percentage of senescent cells in HGPS fibroblasts (Fig. 5i-p). Overall, these data demonstrate that modulation of mitotic efficiency through FoxM1 induction in elderly and HGPS cells prevents both aneuploidy and cellular senescence.

Aneuploidy is a hallmark of elderly senescent cells

Experimental modulation of FoxM1 levels in the young (FoxM1 RNAi) and elderly fibroblasts (FoxM1-dNdK) underlined aneuploidy and senescence to be inherently linked. Previous studies have found mouse models of chromosomal instability to exhibit premature aging [11,46], and cellular models of CIN to induce senescence [47]. Though informative, these studies suffer the drawbacks that CIN-inducing single gene editing leads to higher aneuploidy levels than those accumulating during normal aging, and is a non-physiological stress either present from early development onward (mouse models) or acutely induced (cellular models). Whether the mild aneuploidy levels associated with global transcriptional shutdown of mitotic genes account for cellular senescence in natural aging remains unknown. To address this question, we FACS-sorted senescent cells from neonatal or elderly fibroblast cultures using SA-β-gal as a senescence marker and measured the aneusomy index of three chromosome pairs (Fig. 6a-f). As expected, the percentage of SA-β-gal positive cells was considerably higher in elderly vs. neonatal early passage cell cultures (Fig. 6a,b,e), and consistent with our quantitative analysis using fluorescence microscopy (Supplementary Fig.1d). The aneusomy indexes of SA-β-gal positive cells were significantly higher than those of unsorted controls (Fig. 6f). Extrapolation of the aneusomy indexes to 23 chromosome pairs indicated aneuploidy levels of ~25% and ~70% in

neonatal and elderly cell subpopulations, respectively. Thus, our data indicate that senescent cells from old donors are significantly more aneuploid than senescent cells from young donors, suggesting aneuploidy as a major hallmark of cellular senescence in natural aging. To investigate whether FoxM1 repression is responsible for this difference, we next FACS-sorted SA-β-gal positive cells from siFoxM1-depleted neonatal cell cultures and from octogenarian cell cultures expressing FoxM1-dNdK (Fig. 6c-e). We observed a 4.9x increase of senescent cells, and a comparable 5.3x increase in the aneusomy index, following FoxM1 repression in cells from neonatal donors. Conversely, a 2.2x decrease of senescent cells, and a 1.5x decrease in the aneusomy index was found following FoxM1-dNdK expression. These results demonstrate that FoxM1 levels modulate aneuploidy-driven senescence.

Altogether, our data point up for a positive feedback loop between cellular aging and aneuploidy, in which naturally aged cells with early senescent phenotypes loose mitotic fidelity and generate an aneuploid progeny that primarily accounts for the accumulation of full senescent phenotypes. We show that induction of FoxM1 transcriptional activity in elderly cells ameliorates cell autonomous and non-autonomous feedback effects between mitotic fidelity and senescence (Fig. 6g).

Discussion

Aging is the largest risk factor for most diseases [48]. In recent years, seminal studies have shown that the accumulation of senescent cells in tissues over time shortens healthy lifespan and that selective clearance of senescent cells can greatly postpone aging [32,49]. Our results bring novel insight into how senescent cells arise and provide a molecular basis to prevent senescence and thus, an alternative strategy to emergent senolytic therapies [50].

SASP phenotype in elderly mitotic cells and aneuploidy-driven senescence. Previous studies have suggested G2 and 4N G1 (mitosis skip) as the phase at which senescent cells exit the cell cycle [51,52]. However, these studies made use of the acute senescence stimuli, gamma irradiation and oncogenic Ras overexpression respectively. In contrast to acute senescence, chronic senescence results from long-term, gradual macromolecular damage caused by stresses during lifespan (e.g. loss of proteostasis, DNA damage, epigenetic changes). We demonstrate that in a natural aging cellular model, consisting of dermal fibroblasts retrieved from elderly donors and cultured under limited passage number to prevent replicative *in vitro* aging, senescent cells are mostly aneuploid as a result of defective chromosome mis-segregation. Nonetheless, as shown for oncogene-induced senescence and replicative senescence [52,53], one round of cell division is likely required for a transition from 'early' to fully senescent state. Consistent with this idea of senescent state evolution, we found elderly mitotic cells to express SASP genes. The SASP is largely initiated by p38 MAPK signaling [54], which has been shown to be activated by mitotic delay [55,56], which fits with our observation that mitotic duration steadily increases with aging.

Even though aneuploidy has been correlated with senescence, previous studies have used genetically induced chromosomal instability models or *in vitro* models of acute senescence induction in which the aneuploidy levels are too high in comparison to the mild levels we found in our model of naturally aged cells. Nevertheless, using an innovative experimental setup, we demonstrated that FACS-sorted cells exhibiting high SA-β-gal activity are prominently aneuploid in old samples compared to young samples. We hypothesize this difference to be the result of an aneuploidization propensity of elderly cells, caused by the repression of players of the error-correction machinery for chromosome attachments (Supplementary Table 1).

Molecular mechanism of aging mitotic decline. We showed that the frequency of mitotic

abnormalities increases in older cells resulting in mild aneuploidy levels. We identified FoxM1 transcription factor as the molecular determinant of this age-associated mitotic decline. FoxM1 repression is likely mediated by activation of stress pathways, presumably triggered by primary causes of cellular damage, such as genomic instability or loss of proteostasis. For instance, it has been shown that genotoxic stress can activate the p53-p21-DREAM pathway, which in turn prevents early cell cycle gene expression required for FoxM1 transcriptional activity [43,57].

Transcriptional deregulation during aging has been widely reported in asynchronous cell populations [58,59]. In this study, we used synchronized mitotic populations and found that many cell cycle genes were deregulated in old cells when compared to young cells. Intriguingly, old mitotic cells have intrinsic low levels of mitotic transcripts. While this supports the observed mitotic abnormalities and increased aneuploidy, it is still surprising how elderly mitotic cells can cope with such reduced levels of transcripts (e.g. *CCNB1*). One possibility might be the balanced/stoichiometric repression of most mitotic genes. Furthermore, parallel mechanisms might buffer aging-mediated repression of mitotic transcripts. For example, even though we found SAC genes to be downregulated in elderly cells, SAC functionality was similar in young and old cells, suggesting that a parallel downregulation of genes contributing to proteasome activity (e.g. APC/C subunits) might buffer SAC gene repression (Supplementary Table 1).

Modulation of FoxM1 activity to ameliorate cellular aging phenotypes. We demonstrate that reestablishment of FoxM1 expression in elderly and HGPS fibroblasts can rescue mitotic decline and aneuploidy-driven senescence. Fibroblasts are the main constituents of connective tissue and are important players in extracellular matrix production and tissue repair. Therefore, preventing the accumulation of senescent fibroblasts will counteract a SASP-induced inflammatory microenvironment in these tissues, and will help to protect stem cell and parenchymal cell

functions. Re-expression of FoxM1 could thus protect against adult stem cell and post-mitotic tissue aging. Indeed, increased expression of one FoxM1 transcriptional target, BubR1 [43], was previously shown to prevent aneuploidization and delay aging [13]. However, other aneuploidy mouse models have not been reported to exhibit premature aging. Possible explanations are the premature sacrifice of mice before they start developing aging phenotypes later in life and the cursory analysis for overt age-related degeneration missing tissue-specific phenotypes [14]. Alternatively, aneuploidy-associated genes that are strongly linked with early aging might require induction of mild levels of aneuploidy or counteracting functions in additional cellular stresses that engage senescence response pathways. This appears to be the case of FoxM1. Not only FoxM1 repression translates into mild aneuploidy levels, but also FoxM1 might further act by counteracting age-associated cellular damage caused by genotoxic and oxidative stresses [42,60]. Interestingly, increased FoxM1 expression was shown to improve liver-regenerating capacity in older mice [41] and lung regeneration following injury [61] without being tumorigenic, reinforcing that transcriptional modulation of mitotic fidelity could become a powerful therapy against aging and progeria syndromes, with advantages over other emergent strategies [50,62]. Not only it would circumvent the risks associated with cellular reprogramming to pluripotency, but it would also prevent senescent cell accumulation and thus avoid any irreversible deterioration of tissue extracellular matrix, which can not be rescued by senolysis [32]. Thus, our findings disclose a molecular mechanism with clinical benefit to healthy lifespan extension and HGPS treatment.

Acknowledgments

All data are archived at the i3S Institute. We thank H. Maiato, J.M. Cabral and J. Bessa at i3S for critical discussions and reading of the manuscript; P. Sampaio and A. Maia for technical help

with Advanced Light Microscopy. E.L. holds an FCT Investigator Postdoctoral Grant (IF/00916/2014) from FCT/MCTES (Fundação para a Ciência e a Tecnologia/Ministério da Ciência, Tecnologia e Ensino Superior). FCT Fellowship (SFRH/BD/74002/2010) supported J.C.M. The following project grants supported this work: PTDC/BEX-BCM/2090/2014 funded by FCT; NORTE-01-0145-FEDER-000029 funded by North Regional Operational Program (NORTE2020) under PORTUGAL 2020 Partnership Agreement through Regional Development Fund (FEDER); NORTE-07-0124-FEDER-000003 co-funded by North Regional Operational Program (ON.2) through FEDER and by FCT; and POCI-01-0145-FEDER-007274 i3S framework project co-funded by COMPETE 2020/PORTUGAL 2020 through FEDER and by FCT; Foundation Pediatric Oncology Groningen grant and Dutch Cancer Society grant 2012-RUG-5549 to FF.

Author Contributions

J.C.M. initiated the project. J.C.M, S.V. and R.R. designed and performed the experiments, and analyzed the data. B.B. and P.B. performed RNA-sequencing and bioinformatics analysis. J.M.E. performed telomeric-FISH analysis. M.G.F., R.M. and F.F. contributed to the study design and edited the manuscript. E.L. conceived the idea, supervised the work and wrote the manuscript. All authors discussed results, prepared Fig.s and edited the manuscript.

Competing Financial Interest

The authors declare no competing financial interests.

Correspondence and requests for materials should be addressed to E.L. (elsa.logarinho@ibmc.up.pt).

342

343 **References:**

344 1. Jacobs, P. A. & Court Brown, W. M. Age and chromosomes. *Nature* **212,** 823–4 (1966).

345 2. Nagaoka, S. I., Hassold, T. J. & Hunt, P. A. Human aneuploidy: mechanisms and new
346 insights into an age-old problem. *Nat. Rev. Genet.* **13,** 493–504 (2012).

347 3. Stone, J. F. & Sandberg, A. A. Sex chromosome aneuploidy and aging. *Mutat. Res.*
348 *DNAging* **338,** 107–113 (1995).

349 4. Dumanski, J. P. *et al.* Mutagenesis. Smoking is associated with mosaic loss of
350 chromosome Y. *Science* **347,** 81–3 (2015).

351 5. Guttenbach, M., Schakowski, R. & Schmid, M. Aneuploidy and ageing: sex chromosome
352 exclusion into micronuclei. *Hum. Genet.* **94,** 295–8 (1994).

353 6. Mukherjee, A. B., Alejandro, J., Payne, S. & Thomas, S. Age-related aneuploidy analysis
354 of human blood cells in vivo by fluorescence in situ hybridization (FISH). *Mech. Ageing*
355 *Dev.* **90,** 145–56 (1996).

356 7. Mukherjee, A. B. & Thomas, S. A longitudinal study of human age-related chromosomal
357 analysis in skin fibroblasts. *Exp. Cell Res.* **235,** 161–169 (1997).

358 8. Carere, A. *et al.* Analysis of chromosome loss and non-disjunction in cytokinesis-blocked
359 lymphocytes of 24 male subjects. *Mutagenesis* **14,** 491–6 (1999).

360 9. Geigl, J. B. *et al.* Analysis of gene expression patterns and chromosomal changes
361 associated with aging. *Cancer Res.* **64,** 8550–7 (2004).

362 10. Ly, D. H., Lockhart, D. J., Lerner, R. A. & Schultz, P. G. Mitotic misregulation and

363 human aging. *Science* **287,** 2486–92 (2000).

364 11. Baker, D. J. *et al.* BubR1 insufficiency causes early onset of aging-associated phenotypes
365 and infertility in mice. *Nat. Genet.* **36,** 744–9 (2004).

366 12. Wijshake, T. *et al.* Reduced Life- and Healthspan in Mice Carrying a Mono-Allelic
367 BubR1 MVA Mutation. *PLoS Genet.* **8,** e1003138 (2012).

368 13. Baker, D. J. *et al.* Increased expression of BubR1 protects against aneuploidy and cancer
369 and extends healthy lifespan. *Nat. Cell Biol.* **15,** 96–102 (2013).

370 14. Ricke, R. M. & van Deursen, J. M. Aneuploidy in health, disease, and aging. *J. Cell Biol.*
371 **201,** 11–21 (2013).

372 15. Gordon, D. J., Resio, B. & Pellman, D. Causes and consequences of aneuploidy in cancer.
373 *Nat. Rev. Genet.* **13,** 189–203 (2012).

374 16. Tang, Y. C. & Amon, A. Gene copy-number alterations: A cost-benefit analysis. *Cell* **152,**
375 394–405 (2013).

376 17. Williams, B. R. *et al.* Aneuploidy affects proliferation and spontaneous immortalization in
377 mammalian cells. *Science* **322,** 703–9 (2008).

378 18. Thorburn, R. R. *et al.* Aneuploid yeast strains exhibit defects in cell growth and passage
379 through START. *Mol. Biol. Cell* **24,** 1274–89 (2013).

380 19. Torres, E. M. *et al.* Effects of aneuploidy on cellular physiology and cell division in
381 haploid yeast. *Science* **317,** 916–24 (2007).

382 20. Sheltzer, J. M., Torres, E. M., Dunham, M. J. & Amon, A. Transcriptional consequences
383 of aneuploidy. *Proc. Natl. Acad. Sci. U. S. A.* **109 VN-,** 12644–12649 (2012).

21. Sheltzer, J. M. *et al.* Aneuploidy drives genomic instability in yeast. *Science* **333,** 1026–30 (2011).

22. Zhu, J., Pavelka, N., Bradford, W. D., Rancati, G. & Li, R. Karyotypic determinants of chromosome instability in Aneuploid budding yeast. *PLoS Genet.* **8,** e1002719 (2012).

23. Blank, H., Sheltzer, J., Meehl, C. & Amon, A. Mitotic entry in the presence of DNA damage is a widespread property of aneuploidy in yeast. *Mol. Biol. Cell* **26,** 2031–2037 (2015).

24. Oromendia, A. B., Dodgson, S. E. & Amon, A. Aneuploidy causes proteotoxic stress in yeast. *Genes Dev.* **26,** 2696–708 (2012).

25. Stingele, S., Stoehr, G. & Storchova, Z. Activation of autophagy in cells with abnormal karyotype. *Autophagy* **9,** 246–8 (2013).

26. Donnelly, N., Passerini, V., Dürrbaum, M., Stingele, S. & Storchová, Z. HSF1 deficiency and impaired HSP90-dependent protein folding are hallmarks of aneuploid human cells. *EMBO J.* **33,** 2374–87 (2014).

27. Macedo, J. C., Vaz, S. & Logarinho, E. Mitotic Dysfunction Associated with Aging Hallmarks. *Adv. Exp. Med. Biol.* **1002,** 153–188 (2017).

28. Goldman, R. D. *et al.* Accumulation of mutant lamin A causes progressive changes in nuclear architecture in Hutchinson-Gilford progeria syndrome. *Proc. Natl. Acad. Sci. U. S. A.* **101,** 8963–8 (2004).

29. Cristofalo, V. J., Allen, R. G., Pignolo, R. J., Martin, B. G. & Beck, J. C. Relationship between donor age and the replicative lifespan of human cells in culture: a reevaluation. *Proc. Natl. Acad. Sci. U. S. A.* **95,** 10614–9 (1998).

406 30. Childs, B. G., Durik, M., Baker, D. J. & van Deursen, J. M. Cellular senescence in aging
407 and age-related disease: from mechanisms to therapy. *Nat. Med.* **21,** 1424–1435 (2015).

408 31. Dimri, G. P. *et al.* A biomarker that identifies senescent human cells in culture and in
409 aging skin in vivo. *Proc. Natl. Acad. Sci. U. S. A.* **92,** 9363–7 (1995).

410 32. Baker, D. J. *et al.* Clearance of p16Ink4a-positive senescent cells delays ageing-associated
411 disorders. *Nature* **479,** 232–6 (2011).

412 33. Rodier, F. & Campisi, J. Four faces of cellular senescence. *Journal of Cell Biology* **192,**
413 547–556 (2011).

414 34. Hayashi, M. T., Cesare, A. J., Rivera, T. & Karlseder, J. Cell death during crisis is
415 mediated by mitotic telomere deprotection. *Nature* **522,** 492–6 (2015).

416 35. Galli, M. & Morgan, D. O. Cell Size Determines the Strength of the Spindle Assembly
417 Checkpoint during Embryonic Development. *Dev. Cell* **36,** 344–52 (2016).

418 36. Cimini, D. *et al.* Merotelic kinetochore orientation is a major mechanism of aneuploidy in
419 mitotic mammalian tissue cells. *J. Cell Biol.* **153,** 517–27 (2001).

420 37. Aird, K. M. *et al.* HMGB2 orchestrates the chromatin landscape of senescence-associated
421 secretory phenotype gene loci. *Journal of Cell Biology* **215,** 325–334 (2016).

422 38. Müller, G. A., Stangner, K., Schmitt, T., Wintsche, A. & Engeland, K. Timing of
423 transcription during the cell cycle: Protein complexes binding to E2F, E2F/CLE,
424 CDE/CHR, or CHR promoter elements define early and late cell cycle gene expression.
425 *Oncotarget* (2016). doi:10.18632/oncotarget.10888

426 39. Sadasivam, S., Duan, S. & DeCaprio, J. A. The MuvB complex sequentially recruits B-
427 Myb and FoxM1 to promote mitotic gene expression. *Genes Dev.* **26,** 474–89 (2012).

40. Laoukili, J. *et al.* FoxM1 is required for execution of the mitotic programme and chromosome stability. *Nat. Cell Biol.* **7,** 126–36 (2005).

41. Wang, X. *et al.* Increased levels of forkhead box M1B transcription factor in transgenic mouse hepatocytes prevent age-related proliferation defects in regenerating liver. *Proc. Natl. Acad. Sci. U. S. A.* **98,** 11468–73 (2001).

42. Smirnov, A. *et al.* FOXM1 regulates proliferation, senescence and oxidative stress in keratinocytes and cancer cells. *Aging (Albany. NY).* **8,** 1384–97 (2016).

43. Fischer, M., Grossmann, P., Padi, M. & DeCaprio, J. A. Integration of TP53, DREAM, MMB-FOXM1 and RB-E2F target gene analyses identifies cell cycle gene regulatory networks. *Nucleic Acids Res.* **44,** 6070–86 (2016).

44. Laoukili, J. *et al.* Activation of FoxM1 during G2 requires cyclin A/Cdk-dependent relief of autorepression by the FoxM1 N-terminal domain. *Mol. Cell. Biol.* **28,** 3076–87 (2008).

45. Laoukili, J., Alvarez-Fernandez, M., Stahl, M. & Medema, R. H. FoxM1 is degraded at mitotic exit in a Cdh1-dependent manner. *Cell Cycle* **7,** 2720–6 (2008).

46. Baker, D. J. *et al.* Early aging-associated phenotypes in Bub3/Rae1 haploinsufficient mice. *J. Cell Biol.* **172,** 529–40 (2006).

47. Andriani, G. A. *et al.* Whole Chromosome Instability induces senescence and promotes SASP. *Sci. Rep.* **6,** 35218 (2016).

48. Partridge, L. Intervening in ageing to prevent the diseases of ageing. *Trends Endocrinol. Metab.* **25,** 555–557 (2014).

49. Behrens, A., van Deursen, J. M., Rudolph, K. L. & Schumacher, B. Impact of genomic damage and ageing on stem cell function. *Nat. Cell Biol.* **16,** 201–7 (2014).

450 50. Childs, B. G. *et al.* Senescent intimal foam cells are deleterious at all stages of
451 atherosclerosis. *Science (80-.).* **354,** 472 LP-477 (2016).

452 51. Krenning, L., Feringa, F. M., Shaltiel, I. A., van den Berg, J. & Medema, R. H. Transient
453 activation of p53 in G2 phase is sufficient to induce senescence. *Mol. Cell* **55,** 59–72
454 (2014).

455 52. Johmura, Y. *et al.* Necessary and sufficient role for a mitosis skip in senescence induction.
456 *Mol. Cell* **55,** 73–84 (2014).

457 53. Dikovskaya, D. *et al.* Mitotic Stress Is an Integral Part of the Oncogene-Induced
458 Senescence Program that Promotes Multinucleation and Cell Cycle Arrest. *Cell Rep.* **12,**
459 1483–96 (2015).

460 54. Salminen, A., Kauppinen, A. & Kaarniranta, K. Emerging role of NF-??B signaling in the
461 induction of senescence-associated secretory phenotype (SASP). *Cellular Signalling* **24,**
462 835–845 (2012).

463 55. Uetake, Y. & Sluder, G. Prolonged prometaphase blocks daughter cell proliferation
464 despite normal completion of mitosis. *Curr. Biol.* **20,** 1666–1671 (2010).

465 56. Santaguida, S. & Amon, A. Short- and long-term effects of chromosome mis-segregation
466 and aneuploidy. *Nat. Rev. Mol. Cell Biol.* **16,** 473–485 (2015).

467 57. Anders, L. *et al.* A systematic screen for CDK4/6 substrates links FOXM1
468 phosphorylation to senescence suppression in cancer cells. *Cancer Cell* **20,** 620–34
469 (2011).

470 58. de Magalhães, J. P. *et al.* The Human Ageing Genomic Resources: online databases and
471 tools for biogerontologists. *Aging Cell* **8,** 65–72 (2009).

59. Horvath, S. DNA methylation age of human tissues and cell types. *Genome Biol.* **14,** R115 (2013).

60. Khongkow, P. *et al.* FOXM1 targets NBS1 to regulate DNA damage-induced senescence and epirubicin resistance. *Oncogene* **33,** 4144–55 (2014).

61. Kalinichenko, V. V *et al.* Ubiquitous expression of the forkhead box M1B transgene accelerates proliferation of distinct pulmonary cell types following lung injury. *J. Biol. Chem.* **278,** 37888–94 (2003).

62. Ocampo, A. *et al.* In Vivo Amelioration of Age-Associated Hallmarks by Partial Reprogramming. *Cell* **167,** 1719–1733.e12 (2016).

Methods

Cell culture

A total of 11 human fibroblast cultures, established from skin samples of Caucasian males with ages ranging from neonatal to octogenarian (two biological samples per age), were acquired from cell biobanks as summarized (Supplementary Fig.1A). Several time points over the human lifespan were included to reinforce the validity of any correlation found. All donors were reported as "healthy", except the 8 years-old donor diagnosed with the Hutchison-Gilford progeria. Human dermal fibroblasts (HDFs) were seeded at 1 x 10^4 cells per cm^2 of growth area in minimal essential medium Eagle-Earle (MEM) supplemented with 15% fetal bovine serum (FBS), 2.5 mM L-glutamine and 1x antibiotic-antimycotic (all from Gibco, Thermo Fisher Scientific, CA, USA). Only early passage dividing fibroblasts (population doubling PDL<24) were used in all experiments. *PDL=3.32 (log UCY - log I) + X*, where UCY = the cell yield at

494 that point, l = the cell number used to begin that subculture, and X = the doubling level of the
495 cells used to initiate the subculture being quantitated. Murine adult fibroblasts (MAFs) were
496 cultured in Dulbecco's Modified Eagle Medium (DMEM) supplemented with nutrient mixture F-
497 12, 10% FBS, L-glutamine and antibiotic-antimycotic (all from Gibco). All cells were grown at
498 37 °C and humidified atmosphere with 5% CO_2.
499
500 *Isolation of mouse fibroblasts*
501 Sv/129 mice were housed and handled accordingly to European Union and national legislation.
502 Murine adult fibroblasts were collected from ears of n>3 sv/129 females of the same litter at their
503 age of 8 weeks, 6 months, 1 year, 1.5 years and 2 years. Ears were washed with phosphate-
504 buffered saline (PBS), cut into small pieces, and incubated with 1 mg/ml collagenase D and
505 1 mg/ml collagenase/dispase (both from Roche Applied Science, Germany) in DMEM:F12
506 without FBS, for 45 min at 37 °C and 5% CO_2. Cells were then grown on a 6-well dish
507 containing DMEM:F12, supplemented with 10% FBS and antibiotic-antimycotic.
508
509 *Drug treatments*
510 Fibroblasts were incubated for 24 h in medium containing 2 µg/ml cytochalasin D (C8273,
511 Sigma-Aldrich, MO, USA) to block cytokinesis. For SAC inhibition, cells were treated with
512 5 µM Mps1 inhibitor [63] (AZ3146, TOCRIS, USA). For proteasome activity enhancement, 10 µM
513 of Usp14 inhibitor [64] were used (I-300, BostonBiochem, Cambridge, MA). To measure spindle
514 mispositioning in metaphase cells, proteasome was inhibited with 5 µM MG132 (474790,
515 Calbiochem, CA, USA) for 1.5 h. To inhibit kinesin-5, S-Trityl-L-cysteine (STLC) (2799-07-7,
516 Tocris, USA) was used at different concentrations depending on the experiment: 5 µM during

16 h to enrich the mitotic index for mitotic cell shake-off, and 2.5 µM for 2 h if followed by a washout. Aurora kinase inhibitor ZM447439 (2458, AstraZeneca, Alderley Park, UK) was used at 500 nM for 18 h to artificially induce aneuploidy [65].

Fluorescence in situ hybridization (FISH)

Fibroblasts were grown on Superfrost™ Plus microscope slides (Menzel, Thermo Scientific, CA, USA) placed in a quadriperm dish (Sarsted, Nümbrecht, Germany). In both interphase and binucleated cell FISH, cells were given a hypotonic shock during 30 min (0.03 M sodium citrate, Sigma-Aldrich, MO, USA), followed by fixation in ice-cold Carnoy fixative added drop-wise and incubated for 5 min. This step was repeated two more times. FISH was performed with the Vysis centromeric probes CEP7 Spectrum Aqua, CEP12 Spectrum Green and CEP18 Spectrum Orange (Abbott Laboratories, Chicago, IL, USA) according to manufacturer's instructions. Slides were mounted with mounting medium containing DAPI (Vectashield, Vector Laboratories, CA, USA).

Senescence-associated β-galactosidase assay

In fixed cell analysis, cells were incubated for 90 min in medium with 100 nM Bafilomycin A1 (B1793, Sigma-Aldrich, MO, USA) to induce lysosomal alkalinization. 33 µM of fluorogenic substrate for β-galactosidase, fluorescein di-β-D-galactopyranoside (F2756, Sigma-Aldrich, MO, USA) were then added to the medium, and incubation carried out for 90 min. Cells were fixed in 4% paraformaldehyde for 15 min, rinsed with PBS and permeabilized with 0.1% Triton-X100 in PBS for 15 min. Finally, cells were counterstained with 1 µg/ml DAPI (Sigma-Aldrich, MO, USA). For fluorescence-activated cell sorting, cells were incubated in Bafilomycin A1 as

described above and then exposed to 10 µM of fluorogenic substrate for β-galactosidase, 9H-(1,3-Dichloro-9,9-Dimethylacridin-2-One-7-yl) β-D-Galactopyranoside (DDAOG) for 90 min (Setareh Biotech LLC, USA).

Fluorescence-activated cell sorting (FACS)

FACS was used to isolate subpopulations of senescent (SA-β-gal positive) live fibroblasts. FACS sorting was performed in FACSAria™ I Cell Sorter (BD Biosciences, CA, USA), using the laser-line of 633 nm. All cells within a single experiment were detected using the same voltage settings and sorted using an 85 µm nozzle. Cells were initially gated by forward scatter-area (FSC-A) vs. side scatter-area (SSC-A), which excludes dead cells and subcellular debris, with subsequent exclusion of cell doublets and clumps through FSC-A vs. FSC-width (FSC-W) plot. The signal was detected using the APC-A channel. The relative β-galactosidase activity was inferred from the median fluorescence intensity of the population. The sorting gates were designed accordingly to the respective auto-fluorescent control. Cells were sorted directly into MEM with 15% FBS, and seeded in Superfrost™ Plus microscope slides for subsequent FISH analysis. Analysis of FACS-data was done using FlowJo v10 software (TreeStar, Inc, Ashland, OR).

Immunostaining

Fibroblasts were grown on sterilized glass coverslips coated with 50 µg/ml fibronectin (F1141, Sigma-Aldrich, MO, USA). For analysis of 53BP1 and Cdkn1a/p21 biomarkers, cells were fixed in freshly prepared 4% paraformaldehyde in PBS for 20 min, whereas for spindle angle analysis, cells were fixed in ice-cold methanol for 4 min. Following fixation, cells were rinsed in PBS and

563 permeabilized in PBS + 0.3% Triton-X100 for 7 min. Cells were next blocked in 10% FBS in
564 PBS-T (PBS + 0.05% Tween-20) for 1 h, and then incubated overnight at 4 °C with primary
565 antibodies diluted in PBS-T + 5% FBS as follows: rabbit anti-53BP1 (#4937, Cell Signaling
566 Technology, MA, USA), 1:100; mouse anti-p21 (SC-6246, Santa Cruz Biotechnology, CA,
567 USA), 1:1,000; mouse anti-α-tubulin (T5168, Sigma-Aldrich, MO, USA), 1:1,500; rabbit
568 anti-CP110 (a gift from Mónica Bettencourt-Dias, IGC, Portugal), 1:100. Secondary antibodies
569 AlexaFluor-488 and -568 (Life Technologies CA, USA) were diluted 1:1,500 in PBS-T + 5%
570 FBS. DNA was counterstained with 1 µg/ml DAPI (Sigma-Aldrich, MO, USA). Coverslips were
571 mounted in slides with mounting solution (90% glycerol, 0.5% N-propyl-gallate, 20 nM Tris,
572 pH 8).
573
574 *Telomere PNA FISH*
575 Fibroblasts were incubated in 0.05 µg/ml colcemid (15212012, Gibco, Thermo Fisher Scientific,
576 CA, USA) for 4 h, to induce metaphase arrest. Following trypsinization, fibroblasts were
577 incubated in 0.03 M sodium citrate for 30 min at 37 ºC. Cells were then fixed in freshly made
578 Carnoy fixative solution and stored at 4 °C. Metaphase spreads were fixed with 4%
579 formaldehyde in PBS for 2 min, followed by pepsin digestion (1 mg/ml) for 10 min at 37 ºC.
580 After a dehydration step with ethanol, dried slides were hybridized with Telomere-PNA probe
581 (Applied Biosystems, CA, USA) (0.5 µg/ml) in 10 mM Tris pH 7.5, 70% formamide, 0.25%
582 blocking reagent (Roche, Germany), 2 mM $MgCl_2$, 700 µM citric acid, 7 mM Na_2HPO_4, for
583 3 min in a hot plate at 80 ºC and then for 2 h at 37 ºC in humidified chamber. Slides were washed
584 in 70% formamide, 10 mM Tris, 0.1% BSA twice for 15 min, then washed 3 times in Tris-

585 buffered saline (TBS) for 5 min, and finally mounted with mounting media containing DAPI
586 (Vectashield, Vector Laboratories, CA, USA).
587
588 *Microscopy and image analysis*
589 *Phase-contrast live cell imaging.* Fibroblasts were grown in glass-bottom 35mm µ-dishes (Ibidi
590 GmbH, Germany), coated with 50 µg/ml fibronectin (F1141, Sigma-Aldrich, MO, USA). Images
591 were acquired on a Zeiss Axiovert 200M inverted microscope (Carl Zeiss, Oberkochen,
592 Germany) equipped with a CoolSnap camera (Photometrics Tucson, USA), XY motorized stage
593 and NanoPiezo Z stage, under controlled temperature, atmosphere and humidity. Neighbor fields
594 (20-25) were imaged every 2.5 min for 2-3 days, using a 20x 0.3NA A-Plan objective. Stitching
595 of neighboring fields was done using the plugin "Stitch Grid" (Stephan Preibisch) from
596 ImageJ/Fiji software.
597 *Spinning-disk confocal microscopy.* Four-dimensional data sets were collected with Andor
598 Revolution XD spinning-disk confocal system (Andor Technology, Belfast, UK), equipped with
599 an electron multiplying CCD iXonEM Camera and a Yokogawa CSU 22 unit based on an
600 Olympus IX81 inverted microscope (Olympus, Southend-on-Sea, UK). Two laser lines at 488
601 and 561 nm were used for the excitation of GFP and mCherry and the system was driven by
602 Andor IQ software. Z-stacks (0.8-1.0 µm) covering the entire volume of the mitotic cells were
603 collected every 1.5 min with a PlanApo 60x 1.4NA objective. All images represent maximum-
604 intensity projections of all z planes. ImageJ/Fiji software was used to edit the movies.
605 *Fluorescence microscopy*. Analysis of the SA-β-galactosidase fluorescence assay was carried out
606 on a Zeiss AxioImager Z1 (Carl Zeiss, Oberkochen, Germany) equipped with an Axiocam MR
607 and using an EC-Plan-Neofluor 40x 1.3NA objective. Cells displaying >5 fluorescent granules

608 were considered positive for SA-β-gal activity. Calculation of spindle angle in relation to growth
609 surface was done in images acquired as optimal distance z-stacks on a Zeiss AxioImager Z1
610 using a Plan-Apochromat 63x 1.4NA objective. AutoQuant X2 (Media Cybernetics, Rockville,
611 USA) was used for image deconvolution and generation of different axes projections.
612 *Automated microscopy*. Image fields of 53BP1/p21 double immunostaining and FISH staining
613 were acquired on IN Cell Analyzer 2000 (GE Healthcare, UK), equipped with a Photometrics
614 CoolSNAP K4 camera and using a Nikon 20x 0.45NA Plan Fluor objective. Fluorescence
615 intensity thresholds were set by eye and used consistently for samples within each experiment.
616 *Image analysis.* Fixed cell experiments (FISH, SA biomarkers and micronuclei) were blindly
617 quantified using ImageJ/Fiji software. Mitotic duration, asynchronous daughter cell adherence
618 and cytokinesis failure were quantified from phase-contrast movies. Quantifications in Fig. 2e
619 and Fig. 2g were from spinning-disk confocal movies.
620
621 *Western blotting*
622 Mitotic cell populations were collected by shaking off cell culture flasks enriched for mitotic
623 index (MI) by a 16 h treatment with STLC. MI>95% was determined by visual scoring of cells
624 with condensed chromosomes after Carnoy fixation, followed by with 1 µg/ml DAPI in PBS.
625 Lysis buffer (150 nM NaCl, 10 nM Tris-HCl pH 7.4, 1 nM EDTA, 1 nM EGTA, 0.5% IGEPAL)
626 with protease inhibitors was added to mitotic cell pellets, and lysates quantified for protein
627 content by the Lowry Method (DC™ Protein Assay, BioRad, CA, USA). 20 µg of total extract
628 were then loaded in SDS-PAGE gels and transferred onto nitrocellulose membranes for western
629 blot analysis. Membranes were blocked during 1 h with TBS containing 5% low-fat milk.
630 Primary antibodies were diluted in TBS containing 2% low-fat milk as follows: rabbit anti-

631 FoxM1 (#13147, ProteinTech Group Inc, IL, USA), 1:1,000; mouse anti α tubulin (T5168,
632 Sigma-Aldrich, CA, USA), 1:50,000; and mouse anti-GAPDH (#60004, ProteinTech Group Inc,
633 IL, USA), 1:30,000. Goat anti-rabbit (SC-2004, Santa Cruz Biotechnology, CA, USA) and goat
634 anti-mouse (SC-2005, Santa Cruz Biotechnology, CA, USA) HRP-conjugated secondary
635 antibodies were diluted at 1:3,000 in TBS containing 2% low fat milk. Signal was detected using
636 Clarity Western ECL Substrate reagent (Bio-Rad Laboratories, CA, USA) accordingly to
637 manufacturer's instructions. A GS-800 calibrated densitometer with Quantity One 1-D Analysis
638 Softwar 4.6 (Bio-Rad Laboratories, CA, USA) was used for quantitative analysis of protein
639 levels.
640
641 *Lentiviral plasmids*
642 H2B-GFP [66] was amplified as a B*gl*II-H2B-GFP-T2A-B*am*HI-N*ot*I fragment. This PCR
643 fragment was digested with B*gl*II+N*ot*I and ligated into pRetrox-Tight-Puro (Clontech, CA,
644 USA) digested with B*am*HI+N*ot*I, thus destroying the 5' B*am*HI/B*gl*II site while reintroducing a
645 B*am*HI site 3' of H2B-GFP-T2A. In parallel, α-Tubulin [66] was amplified as a B*gl*II-α-Tubulin-
646 B*am*HI-N*ot*I fragment and ligated into pRetrox-Tight-Puro digested with B*am*HI+N*ot*I, again
647 destroying the 5' B*am*HI/B*gl*II site while reintroducing a B*am*HI site 3' of α-Tubulin. mCherry
648 was amplified from pExchange-1-Cherry (Agilent Technologies, CA, USA) as a B*gl*II-mCherry-
649 N*ot*I fragment and was ligated into pRetrox-α-Tubulin digested with B*am*HI-N*ot*I, yielding
650 pRetrox-α-Tubulin-mCherry. Finally, α-Tubulin-mCherry was PCR-amplified as a B*gl*II-α-
651 Tubulin-mCherry-N*ot*I fragment and ligated into pRetrox-H2B-GFP-T2A digested with
652 B*am*HI+N*ot*I, yielding pRetrox-H2B-GFP-T2A-α-Tubulin-mCherry. To obtain pLVX-
653 Tight-Puro-H2B-GFP-T2A-α-tubulin-mCherry, a B*gl*II-H2B-GFP-T2A-α-Tubulin-mCherry-

654 N*ot*I fragment was amplified from pRetroX-H2B-T2A-GFP-α-Tubulin-mCherry and ligated into
655 pLVX-Tight-Puro (Clontech, CA, USA) digested with *BamH*I+*Not*I. To generate
656 pLVX-Tight-Puro-FoxM1dNdK, a B*gl*II-FOXM1-dNdK-*Not*I fragment was amplified from
657 pcDNA3-Flag-ΔN-ΔKEN-FoxM1 [44] and ligated into pLVX-Tight-Puro digested with
658 *BamH*I+*Not*I. Primers used are described in Supplementary Table 3.
659
660 *Lentiviral production and infection*
661 Lentiviruses were produced according to the protocol described in Lenti-X Tet-ON Advanced
662 Inducible Expression System (Clontech). Lentiviruses carrying empty pLVX-Tight-Puro, pLVX-
663 Tight-Puro-H2B-GFP-α-Tubulin-mCherry or pLVX-Tight-Puro-FoxM1dNdK, as well as
664 lentiviruses carrying pLVX-Tet-On Advanced (which expresses rtTA), were generated in
665 HEK293T helper cells transfected with packaging plasmids (pMd2.G and psPAX2) using
666 Lipofectamine 2000 (Life Technologies, Thermo Scientific, CA, USA). Human fibroblasts were
667 co-infected for 12-16 h with responsive and transactivator lentiviruses at 2:1 ratio, in the
668 presence of 8 µg/ml polybrene (AL-118, Sigma-Aldrich, MO, USA). In the following day,
669 750 ng/ml doxycycline (D9891, Sigma-Aldrich, MO, USA) was added to the medium to induce
670 co-transduction. Phenotypes were analyzed and quantified 48-72 h later, and transfection
671 efficiency monitored by scoring the number of fluorescent cells or by western blotting.
672
673 *FoxM1 RNA interference*
674 Cells were transfected 1 h after plating, with 45 nM FoxM1 siRNA (SASI_Hs01_00243977 from
675 Sigma-Aldrich, MO, USA) using Lipofectamine RNAiMAX (Thermo Scientific, CA, USA)

676 according to manufacturer's instructions. Phenotypes were analyzed and quantified 72 h post
677 transfection, and depletion efficiency monitored by western blotting.
678
679 *Real-time PCR*
680 Total RNA was obtained from mitotic fibroblasts (collected as depicted in Fig. 3a and in the
681 Western blotting section) using the RNeasy® Mini kit (Qiagen, Hilden, Germany). RNA purity
682 and integrity was confirmed in the Experion™ system (Bio-Rad Laboratories, CA, USA). cDNA
683 was synthesized from total RNA (1 µg) using iScript Advanced Select cDNA Synthesis kit
684 (BioRad Laboratories, CA, USA). The 2-ΔΔCt method was used to quantify the transcript levels
685 of FOXM1 against the transcript levels of the housekeeping gene (TBP/GAPDH). Primers were
686 designed to span at least one exon-intron junction (Supplementary Table 3). Amplification was
687 performed in a C1000 Touch Thermal Cycler (CFX384 Real-Time System, Bio-Rad
688 Laboratories, CA, USA), and analyzed using CFX Manager Software (Bio-Rad Laboratories,
689 CA, USA).
690
691 *RNA sequencing and bioinformatics*
692 RNA was isolated from mitotic human fibroblasts and validated as described above for
693 PrimePCR assay. RNA-sequencing libraries were prepared using TruSeq Stranded Total RNA
694 with Ribo-Zero Human/Mouse/Rat (RS-122-2201; Illumina, CA, USA) according to
695 manufacturer's protocol. Pooled libraries were sequenced on an Illumina HiSeq 2500 (single-end
696 50 bp). Reads were aligned to the human genome (hg19) using a splicing-aware aligner
697 (StarAligner). Aligned reads were FPM normalized, excluding low abundance genes (mean
698 FPM>1). Differential gene expression analysis was performed using the R-package edgeR

699 (v3.14.0 available from Bioconductor at
700 http://www.bioconductor.org/packages/release/bioc/html/edgeR.html). Significant differential
701 gene expression of aged fibroblasts was defined as *p*-value<0.05 and of genetic manipulations as
702 a 2-logFC cutoff value <-0.7 or >0.7, FDR<0.05 and *p*-value<0.05 (Supplementary Table 1). For
703 generation of RNA-seq heatmaps, FPM normalized read counts were used. Hierarchical
704 clustering was performed using the R library heatmap.2. RNA-seq data of HDF N vs 87y
705 represent two biological replicates of each biological sample from a single experiment. The
706 RNA-seq data from FoxM1 RNAi and dNdK viral infection represent two technical replicates of
707 each biological sample. For ontological analysis, differentially expressed genes were analyzed
708 using Database for Annotation, Visualization and Integrated Discovery (DAVID) Functional
709 Annotation Tool v6.8 [67] (www.david-d.ncifcrf.gov). To calculate the significance of gene set
710 enrichment, empirical p-values were generated using DAVID tool. Genes differentially
711 expressed following FoxM1 RNAi (dataset: 4451 genes) were overlapped with those
712 differentially expressed following FoxM1dNdK expression (dataset: 2,199 genes). Overlap
713 analysis was also performed with a dataset of 249 genes reported as targets of both DREAM and
714 MMB-FoxM1 complexes [43] (Supplementary Table 2). Gene ontology (GO) term enrichment
715 analysis was performed using DAVID Functional Annotation Tool.
716
717 *Statistical Analysis*
718 Sample sizes and statistical tests for each experiment are indicated in the Fig. legends. *p*-values
719 were obtained using GraphPad Prism version 6 (GraphPad, San Diego, CA, USA). Data were
720 tested for parametric vs. non-parametric distribution using D'Agostino-Pearson omnibus
721 normality test. Spearman rank correlation, Mann-Whitney, two-tailed χ^2-square or one-way

ANOVA for multiple comparisons tests were then applied accordingly. ns: $p>0.05$, *$p\leq0.05$, **$p\leq0.01$, ***$p\leq0.001$ and ****$p\leq0.0001$. Values are shown as mean ± s.d. or mean ± s.e.m. When required, box-and-whisker plot with median, IQR and minimum and maximum values was used.

63. Kwiatkowski, N. *et al.* Small-molecule kinase inhibitors provide insight into Mps1 cell cycle function. *Nat. Chem. Biol.* **6,** 359–68 (2010).

64. Lee, B.-H. *et al.* Enhancement of proteasome activity by a small-molecule inhibitor of USP14. *Nature* **467,** 179–84 (2010).

65. Cimini, D., Wan, X., Hirel, C. B. & Salmon, E. D. Aurora kinase promotes turnover of kinetochore microtubules to reduce chromosome segregation errors. *Curr. Biol.* **16,** 1711–8 (2006).

66. Orth, J. D. *et al.* Analysis of mitosis and antimitotic drug responses in tumors by in vivo microscopy and single-cell pharmacodynamics. *Cancer Res.* **71,** 4608–16 (2011).

67. Huang, D. W., Sherman, B. T. & Lempicki, R. A. Systematic and integrative analysis of large gene lists using DAVID bioinformatics resources. *Nat. Protoc.* **4,** 44–57 (2009).

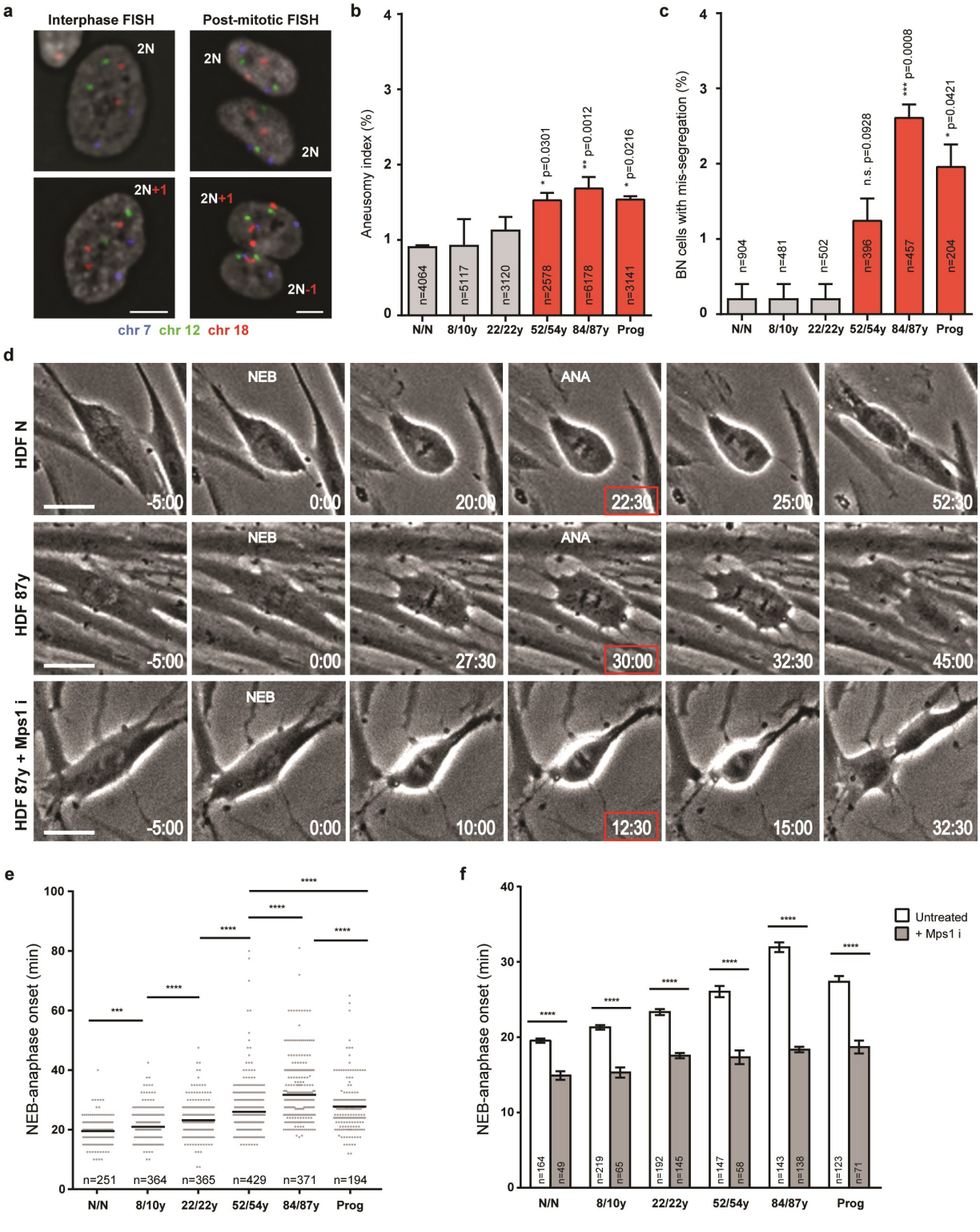

Macedo et al. Figure 1

742 **Figure 1**. **Aneuploidy and mitotic duration increase during normative aging. (a)** FISH in
743 interphase and post-mitotic cells with chromosome-specific centromeric probes as indicated.
744 Representative images of euploid/2N and aneuploid/2N±l cells are shown. Scale bars, 5 μm. **(b)**
745 Aneusomy index in interphase cells from different age donors. **(c)** Percentage of post-mitotic
746 cells with chromosome mis-segregation. **(d)** Frame series of time-lapse phase-contrast movies of
747 mitotic neonatal and elderly cells±Mps1 inhibitor. Mitotic duration was measured from nuclear
748 envelope breakdown (NEB) to anaphase onset (ANA). Time, min:sec. Scale bar, 20 μm. **(e)**
749 Mitotic duration of individual fibroblasts from different donors. **(f)** Mitotic duration under
750 standard conditions as in (e) (white bars) and following treatment with Mps1 inhibitor (gray
751 bars). Values are mean ± s.d. from at least three independent experiments, using two biological
752 samples of similar age (except for progeria). Sample size (n) is indicated in each graph. n.s.
753 $p>0.05$, *$p\leq0.05$, **$p\leq0.01$, ***$p\leq0.001$ and ****$p\leq0.0001$ in comparison to neonatal (N/N) by
754 two-tailed χ^2 (b,c) and Mann-Whitney (e,f) statistical tests.
755
756

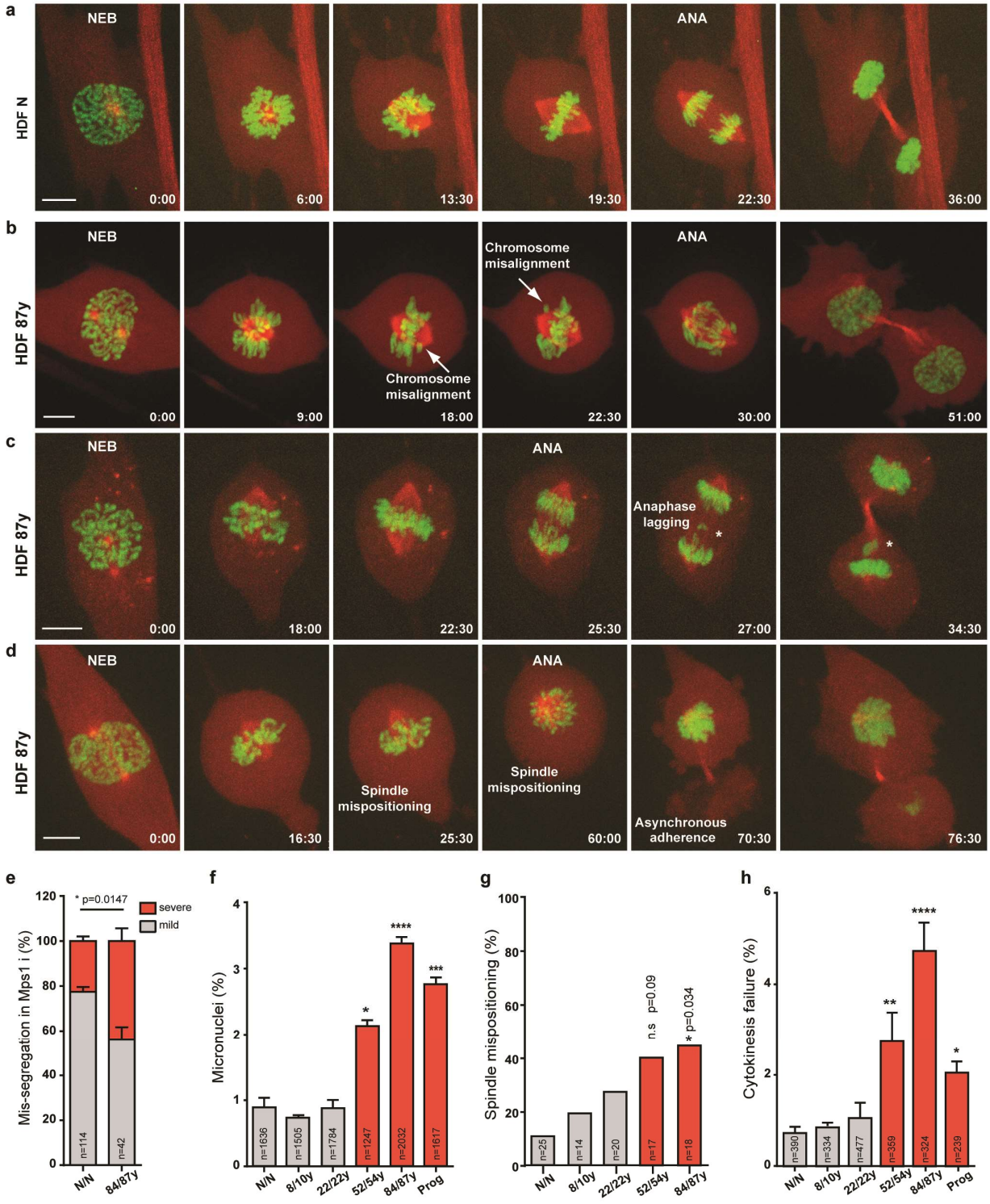

Macedo et al. Figure 2

758 **Figure 2. Mitotic defects associated with advanced age. (a-d)** Frame series of spinning-disk
759 confocal movies of neonatal (HDF N) and elderly (HDF 87y) dividing cells expressing
760 H2B-GFP-α-Tubulin-mCherry. **(a)** Neonatal cell division. **(b-d)** Elderly cell with chromosome
761 alignment delay **(b)**, with anaphase lagging chromosome and micronucleus formation (*) **(c),** or
762 with spindle mispositioning in relation to the growth surface and asynchronous adherence of the
763 daughter cells **(d)** (Supplementary Video 1). Time, min:sec. Scale bar, 5 µm. **(e)** Percentage of
764 cells with mild and severe chromosome mis-segregation following treatment with Mps1
765 inhibitor. **(f)** Percentage of cells with micronuclei. **(g)** Fraction of cells with spindle
766 mispositioning. **(h)** Rate of cytokinesis failure. Values are mean ± s.d. from at least two
767 independent experiments, using two biological samples of similar age (except for progeria).
768 Sample size (n) is indicated in each graph. *$p \leq 0.05$, **$p \leq 0.01$, ***$p \leq 0.001$ and ****$p \leq 0.0001$ in
769 comparison to N/N by two-tailed χ^2 (e-h) and Mann-Whitney (j) statistical tests.
770
771

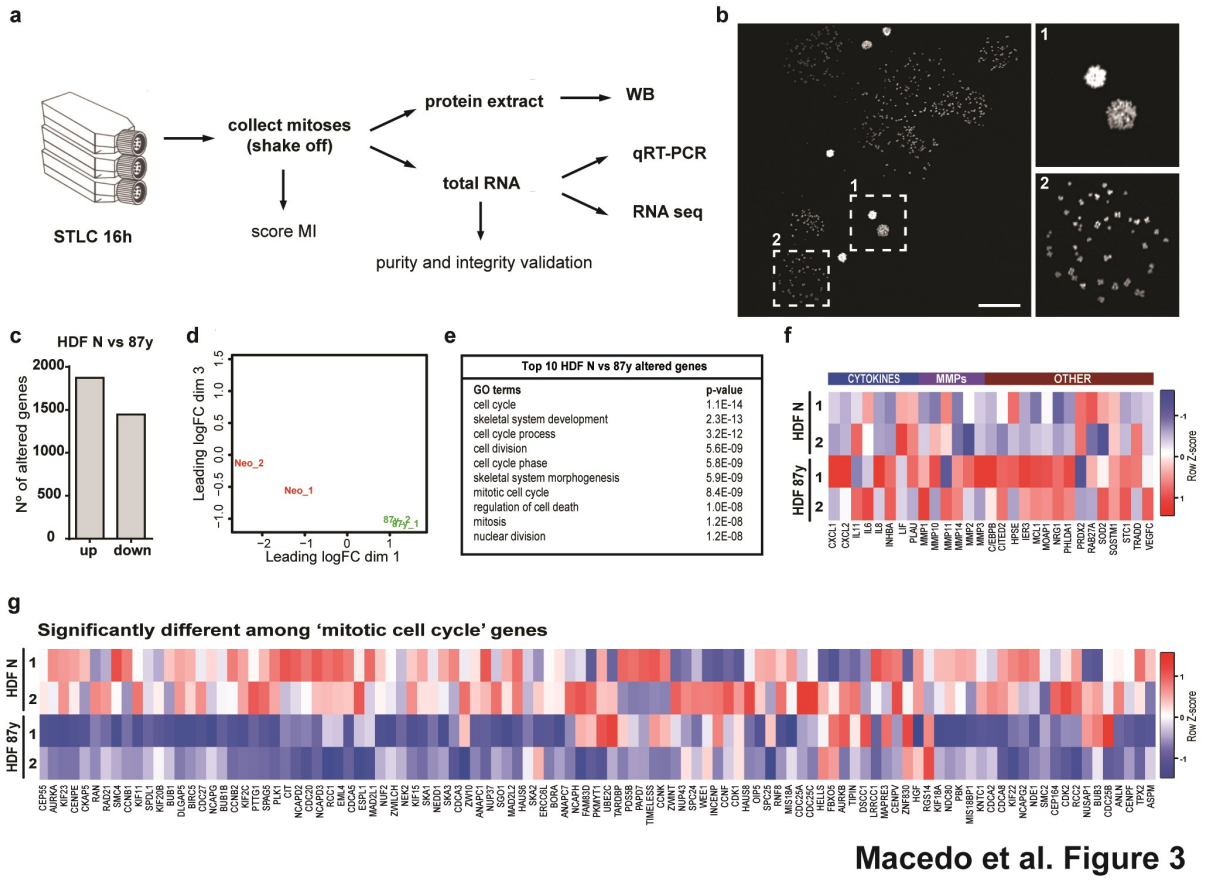

Macedo et al. Figure 3

Figure 3. Elderly mitotic fibroblasts exhibit a downregulation of cell cycle genes. (a) Experimental layout. Fibroblast cultures from different age donors were treated with kinesin-5 inhibitor (STLC) to enrich for mitotic index (MI). Mitotic (detached) cells were collected and inspected for MI>95%. Protein extracts and total RNA were prepared for gene expression analyses. **(b)** Representative image of MI>95%. Scale bar, 100 µm. **(c)** Number of altered genes of HDF 87y, comparing to HDF N. **(d)** Multidimensional scaling plot of distances between gene expression profiles based on sample RNA-sequencing. **(e)** Top ten altered GO terms organized by p-values using the DAVID Functional Annotation tool. **(f)** Heatmap of SASP gene (cytokines, metalloproteinases (MMPs) and other factors) expression in HDF N and HDF 87y. Genes are represented in columns and biological replicates are represented in rows. In the Z-score column, color intensities represent higher (red) to lower (blue) expression. **(g)** Heatmap of genes within

784 the ‘mitotic cell cycle’ GO term differentially expressed (fold change>1.6x; 5%FDR) between
785 HDF N and HDF 87y.
786
787

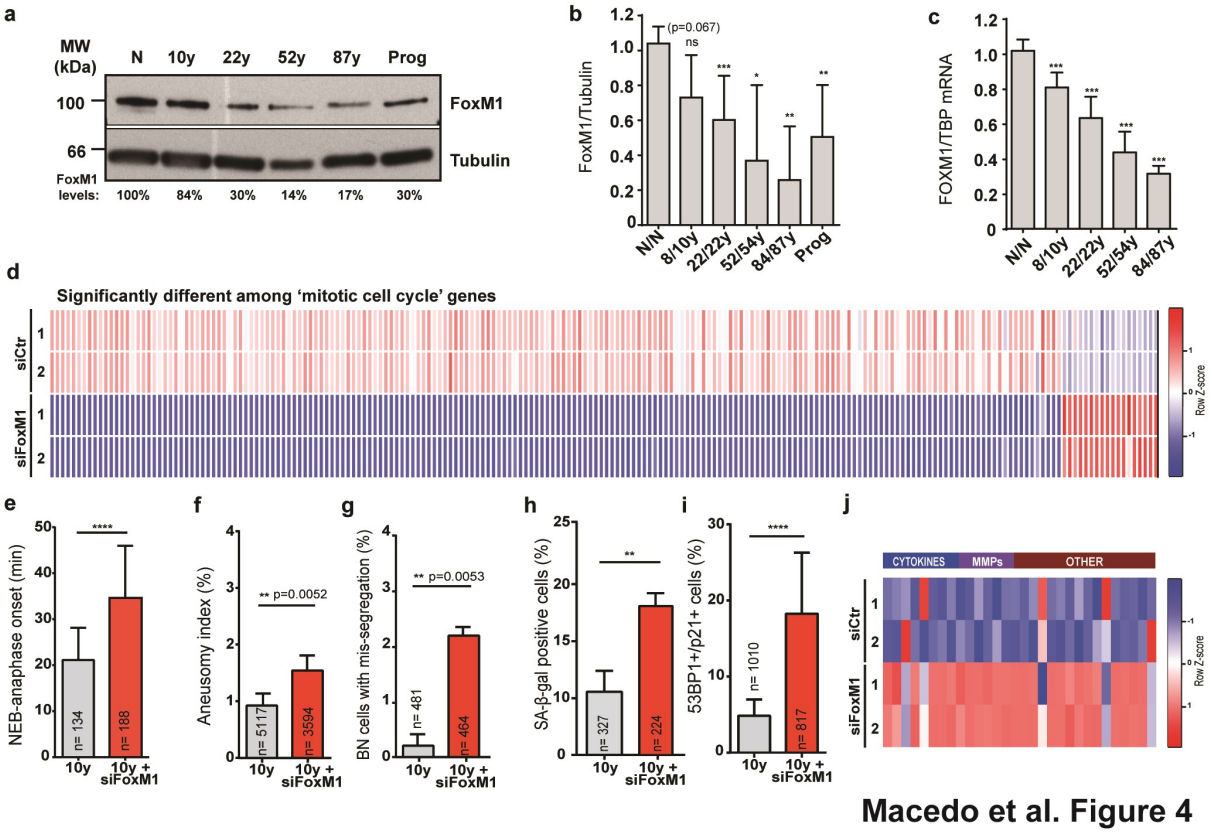

Macedo et al. Figure 4

Figure 4. FoxM1 repression dictates cellular phenotypes associated with aging. (a,b) FoxM1 protein levels in mitotic extracts of different age samples. FoxM1 levels were normalized to α-tubulin levels and to neonatal (N/N). **(c)** *FOXM1* transcript levels in mitotic total RNA from different age samples, normalized to *TBP* transcript levels and compared to neonatal. **(d)** Heatmap of genes within the 'mitotic cell cycle' GO term differentially expressed (fold change>1.6x; 5%FDR) by RNA-seq between control and FoxM1 siRNA-depleted 10 years-old fibroblasts. Genes are represented in columns and sample replicates are represented in rows. In the Z-score column, color intensities represent higher (red) to lower (blue) expression. **(e)** Mitotic duration (NEB-anaphase onset) of control and FoxM1 siRNA-depleted fibroblasts. **(f-g)** Aneusomy index in interphase cells **(f)** and in binucleated cells **(g)**. **(h-i)** Percentage of cells staining positive for the senescence markers β-galactosidase **(h)** and 53BP1/p21 **(i)**. **(j)** Heatmap

800 of SASP genes differentially expressed between HDF 10y and 10y siFoxM1. Values are
801 mean ± s.d. of three independent experiments. Sample size (n) is indicated in each graph.
802 *$p \leq 0.05$, **$p \leq 0.01$, ***$p \leq 0.001$ and ****$p \leq 0.0001$ by Mann-Whitney (b,c,e) and two-tailed χ^2
803 (f, g, h, i) statistical tests.
804
805

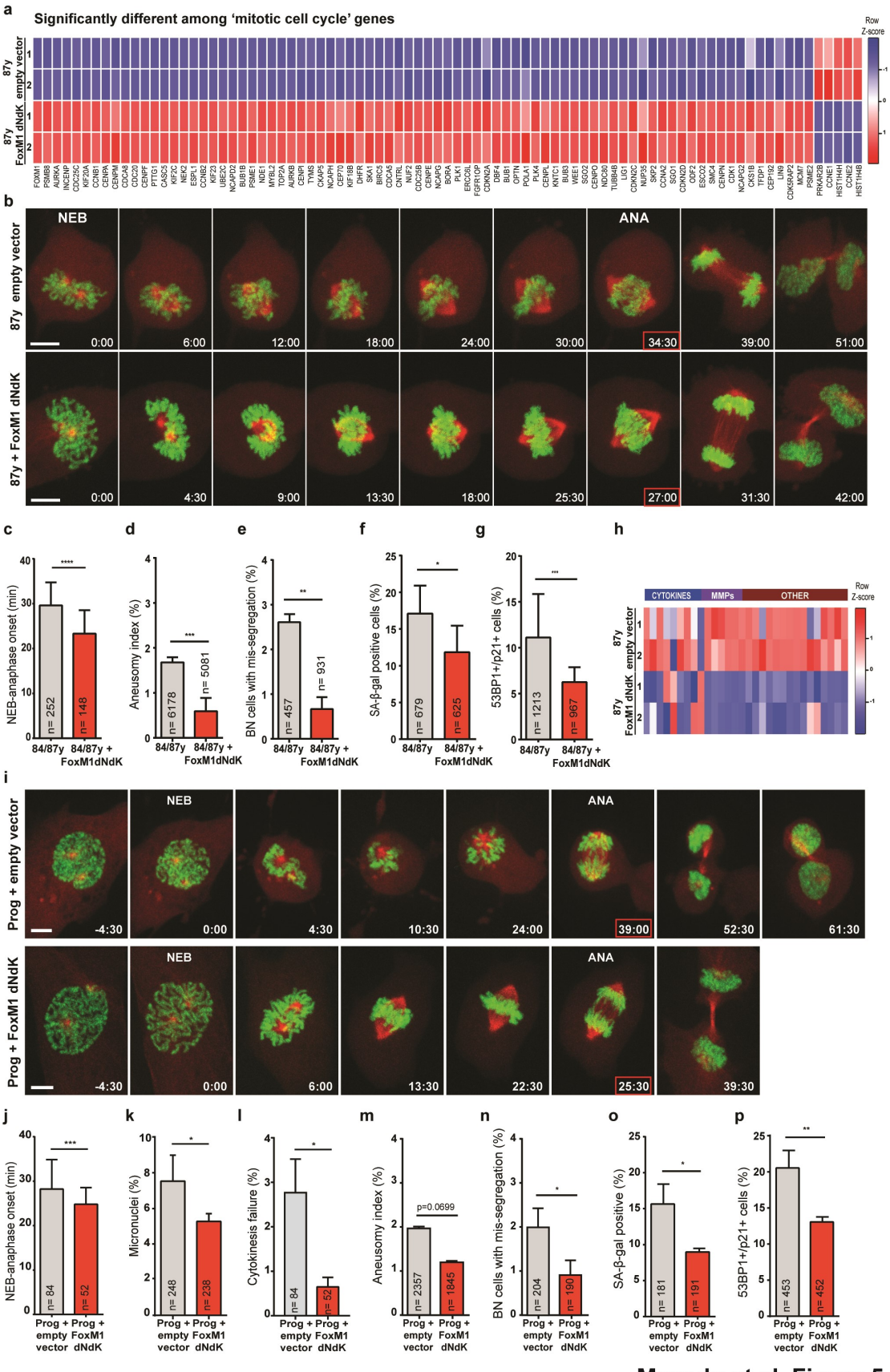

Macedo et al. Figure 5

Figure 5. Constitutively active FoxM1 ameliorates mitotic fitness and aging markers in elderly and HGPS cells. (a) Heatmap of genes within the 'mitotic cell cycle' GO term differentially expressed (fold change>1.6x; 5%FDR) between mitotic elderly cells transduced with lentiviral empty vector or vector expressing FoxM1dNdK. In the Z-score column, color intensities represent higher (red) to lower (blue) expression. **(b)** Movie frames of elderly dividing cells expressing H2B-GFP-α-Tubulin-mCherry (upper panel) and H2B-GFP-α-Tubulin-mCherry + FoxM1dNdK (lower panel) (Supplementary Video 2). Time, min:sec. Scale bar, 5 μm. **(c)** Mitotic duration (NEB to anaphase onset) in elderly fibroblasts infected with control and FoxM1dNdK lentiviruses. **(d-e)** Aneusomy index in interphase **(d)** and binucleated cells **(e)**. **(f-g)** Percentage of cells staining positive for the senescence markers β-galactosidase **(f)** and 53BPl/p2l **(g)**. **(h)** Heatmap of SASP genes differentially expressed between HDF 87y and 87y FoxM1dNdK. **(i)** Movie frames of mitotic HGPS fibroblasts expressing H2B-GFP-α-Tubulin-mCherry (upper panel) and H2B-GFP-α-Tubulin-mCherry+FoxM1dNdK (lower panel) (Supplementary Video 3). Time min:sec. Scale bar, 5 μm. **(j)** Mitotic duration of HGPS fibroblasts transduced with empty and FoxM1dNdK lentiviruses. **(k)** Percentage of cells with micronucleus. **(l)** Percentage of cells failing cytokinesis. **(m)** Aneusomy index in interphase nuclei and **(n)** mis-segregation events in binucleated cells estimated from FISH analysis of 3 chromosome pairs. **(o,p)** Percentage of cells staining positive for the senescence markers **(o)** β-galactosidase and **(p)** 53BP1/p2l. Values are mean ± s.d. of three independent experiments. Sample size (n) is indicated in each graph. *$p \leq 0.05$, **$p \leq 0.01$, ***$p \leq 0.001$ and ****$p \leq 0.0001$ by Mann-Whitney (c,j) and two-tailed χ^2 (d-g; k-p) statistical tests.

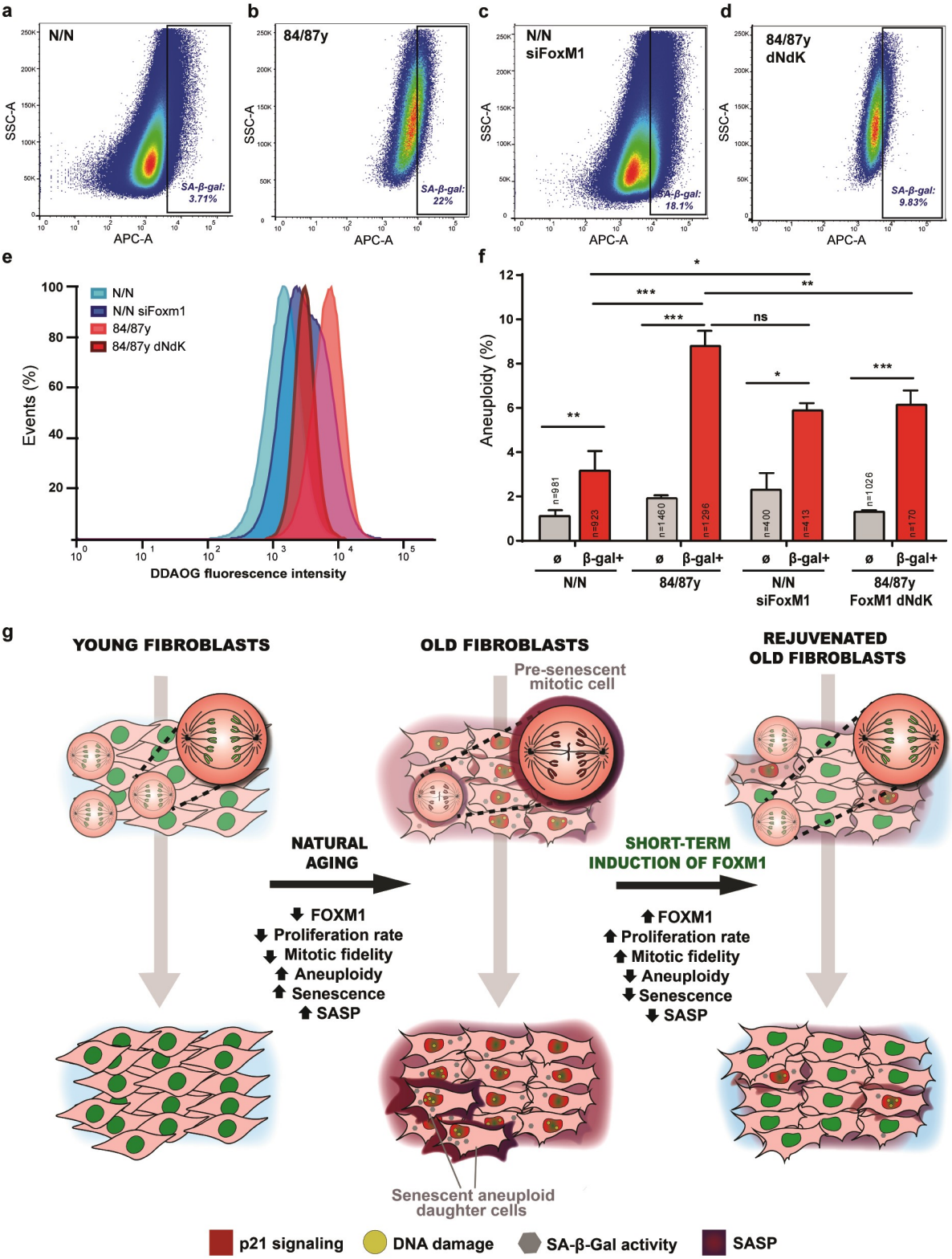

Macedo et al. Figure 6

831 **Figure. 6. FoxM1 governs aneuploidization-driven cellular senescence in elderly cells. (a-d)**
832 FACS sorting of senescent cells from neonatal **(a)**, elderly **(b)**, FoxM1 siRNA-depleted neonatal
833 **(c)** and 84y/87y with FoxM1dNdK **(d)** cell populations with high β-galactosidase activity. The
834 gates were defined accordingly to the respective auto-fluorescent control. **(e)** Relative intensity
835 levels of the fluorogenic substrate DDAOG in the sorted cell populations. **(f)** Aneuploidy index
836 in FACS-sorted β-gal-positive fibroblast subpopulations (β-gal+) vs. unsorted populations (∅) as
837 determined by FISH analysis for 3 chromosome pairs. Values are mean ± s.d. of two independent
838 experiments. Sample size (n) is indicated in each graph. ns: $p>0.05$, *$p\leq0.05$, **$p\leq0.01$,
839 ***$p\leq0.001$ and ****$p\leq0.0001$ by two-tailed χ^2 statistical test. **(g)** Model summarizing the
840 molecular basis of age-associated mitotic decline and accumulation of senescent cells. FoxM1
841 repression in pre-senescent dividing cells leads to aneuploidy, which accounts for the transition
842 into full senescence. FoxM1 induction in old cells restores mitotic fitness and erases aging
843 markers.
844

845 **Supplementary information:**

a

HDFs (age)	Reference	Repository information (PDL at Freeze)	Cumulative PDL (in our experiments)
N	C-0004-5C lot 74812, Invitrogen	X	X+ 1.7/ +3.2 / +8.2
N	DFM021711A, Zen Bio	X	X+2.2 / +4.6 / +7.2
8y	GM08398, Coriell Cell Repository	5.73	7.4 / 11.5 /14.3
10y	GM03348, Coriell Cell Repository	4.2	5.9 / 7.8 / 9.9
22y	DFME102710, Zen Bio	X	X+1.8 / + 2.2 / 3.0
22y	GM23976, Coriell Cell Repository	7.6	9.6 / 11.4 / 13.9/ 15.4
52y	GM28967, Coriell Cell Repository	4.17	5.9 / 7.4 / 8.9 / 10.4
54y	DFM062509, Zen Bio	X	X+1.73 / +3.1 / +4.4
84y	AG11488, Coriell Cell Repository	10	11.8 /13.4 / 15.3 / 17
87y	AG10884, Coriell Cell Repository	7	8.8 / 10.9 / 12.1 / 13.3
8y, HGPS	AG03513, Coriell Cell Repository	15	16.9 / 18.4 / 19.9 / 21.7 / 23.3

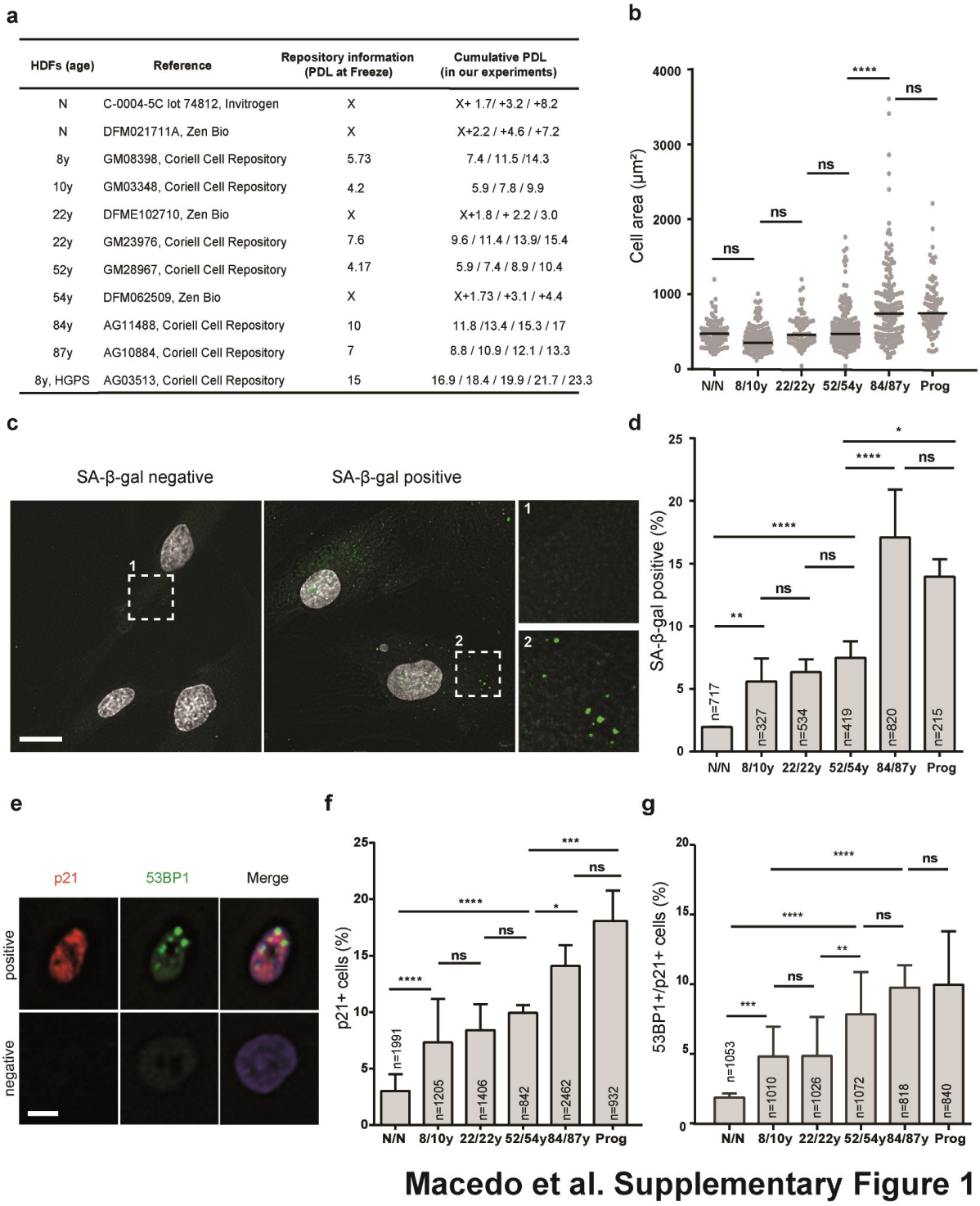

Macedo et al. Supplementary Figure 1

846

847 **Supplementary Figure 1. Senescence markers in human dermal fibroblasts from different**
848 **age donors. (a)** Fibroblasts from skin biopsies of Caucasian males with different ages used in
849 this study. All donors were reported as "healthy", except the 8 years old donor with the
850 Hutchison-Gilford Progeria Syndrome. **(b)** Cellular area. Scatter plots show mean of n>50 cells.
851 **(c)** Representative images of senescence-associated β-galactosidase (SA-β-gal) negative and
852 positive cells. Scale bar, 20 µm. **(d)** Percentage of cells staining positive for senescence-
853 associated β-galactosidase assay. **(e)** Representative images of cell cycle-arrested cells (p21
854 positive) and DNA damage (≥1 53BP1foci). Scale bar, 10 µm. **(f)** Percentage of cells staining
855 positive for Cdkn1a/p21 cell cycle inhibitor. **(g)** Percentage of Cdkn1a/p21 positive cells with
856 53BP1foci. In all graphs, bars represent mean ± s.d. values from three independent experiments
857 using two biological samples of similar age (except for progeria). Sample size (n) is indicated in
858 each graph. ns: $p>0.05$, *$p\leq0.05$, **$p\leq0.01$, ***$p\leq0.001$ and ****$p\leq0.0001$ by two-tailed χ^2 (d, f,
859 g) and Mann-Whitney (b) statistical tests.
860
861

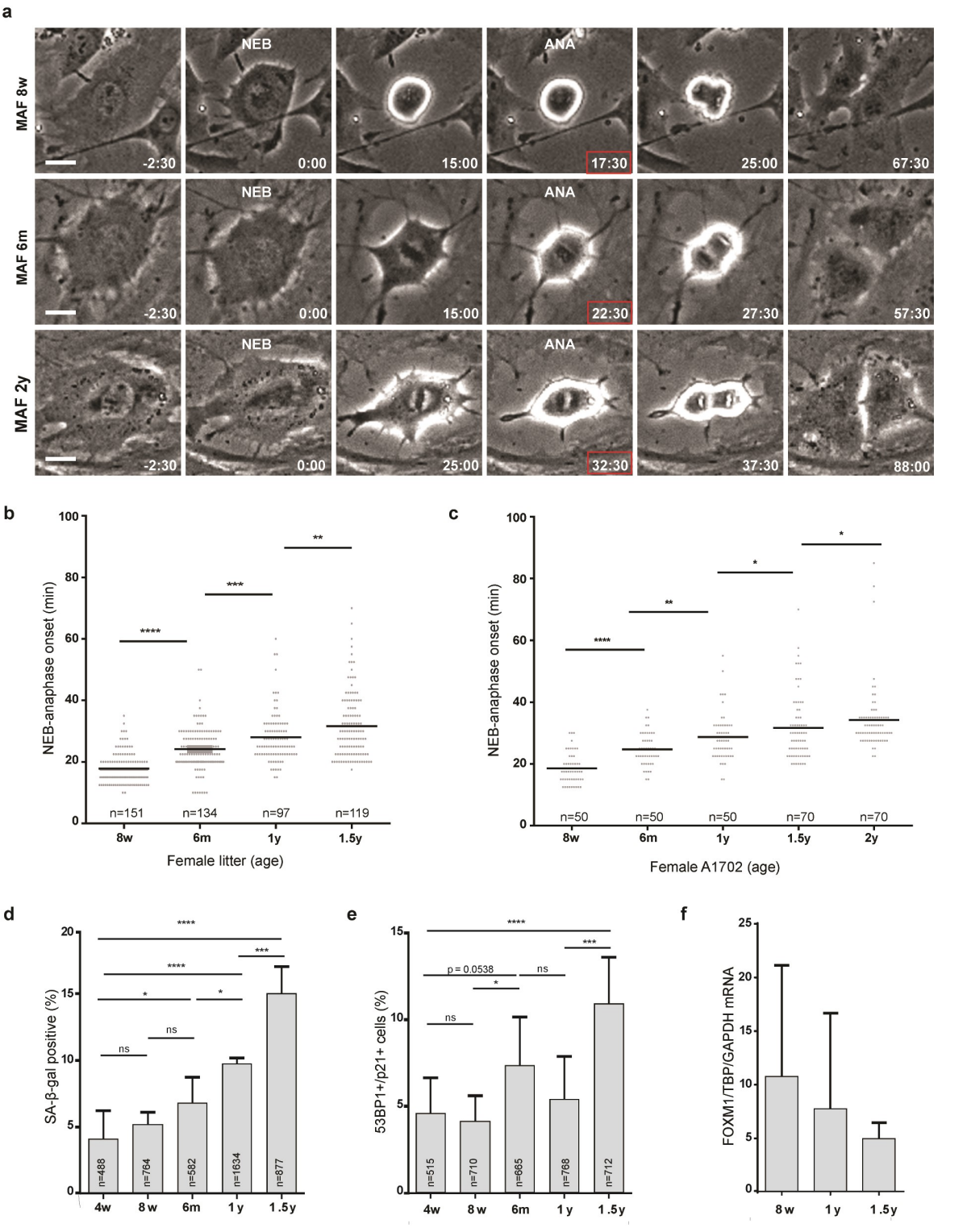

Macedo et al. Supplementary Figure 2

862

Supplementary Figure 2. Aging-associated mitotic delay in mouse fibroblasts. (a) Movie frames of mitosis in MAFs collected at different age time-points as indicated. NEB, nuclear envelope breakdown. ANA, anaphase onset. Time min:sec. Scale bar, 20 µm. **(b)** Mitotic duration (NEB to anaphase onset) of individual MAFs collected at different age time-points from ≥3 sv/129 sister females. **(c)** Mitotic duration of individual MAFs collected at different age time-points from one randomly chosen single female (Al702). **(d)** Percentage of cells staining positive for senescence-associated β-galactosidase assay. **(e)** Percentage of Cdkn1a/p21 positive cells with 53BP1foci. **(f)** *FOXM1* transcript levels in mitotic total RNA from different age samples. Values are mean ± s.d. normalized to *TBP* and *GAPDH* transcript levels. Values are shown as mean, and sample size (n) is indicated in each graph. ns: $p>0.05$, *$p\leq0.05$, **$p\leq0.01$, ***$p\leq0.001$ and ****$p\leq0.0001$ by Mann-Whitney statistical test.

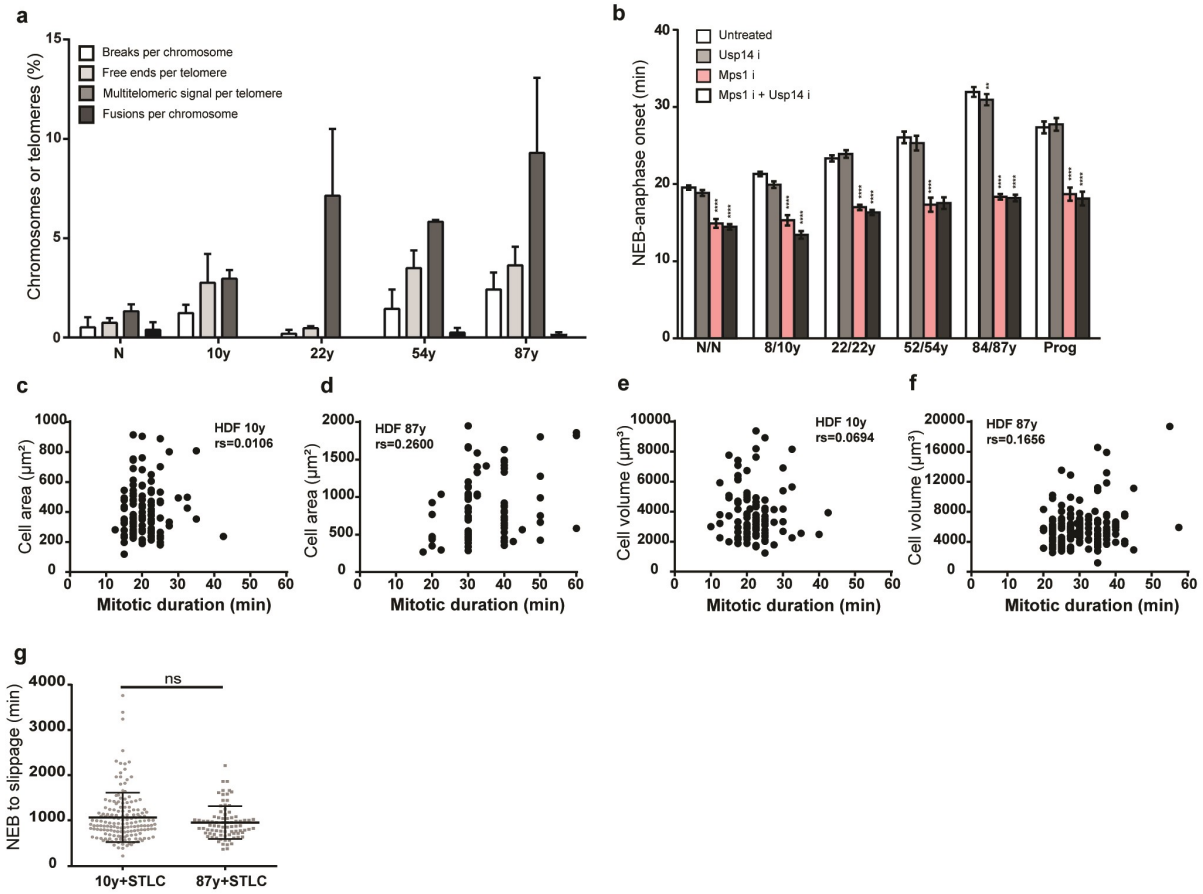

Macedo et al. Supplementary Figure 3

Supplementary Figure 3. Effects of SAC activity, proteotoxic stress and cell size in mitotic duration. (a) Metaphase spreads of colcemid-treated cells of different age donors were quantified for chromosome fusions, chromosome breaks, telomere free ends and multitelomeric signals (MTS; marker of telomere replication defect). At least 900 chromosomes or 3,500 telomeres were quantified in two independent experiments. Values are shown as mean ± s.e.m. Age-dependent significant differences in chromosome aberrations were tested by one-way ANOVA for linear trend and multiple comparisons. Chromosome fusions, chromosome breaks and telomere free ends, not significant; MTS shown a linear trend with p-value≤0.05. **(b)** Mitotic duration of human fibroblasts from different age donors cultured under standard conditions (white bars) and following treatment with Usp14 inhibitor (light gray bars), Mps1 inhibitor

887 (colored bars) and Mps1+Usp14 inhibitors (dark gray bars). **(c-f)** Spearman's correlation
888 coefficients (r_s) between mitotic duration and **(c-d)** cell area or **(e-f)** cell volume. **(g)** Elapsed
889 time from nuclear envelope breakdown (NEB) to cell's adherence into the surface (slippage) in
890 fibroblasts treated with kinesin-5 inhibitor (STLC). Values are mean ± s.d. of n>50 (b) and n>80
891 (c-g) scored cells from three independent experiments. ns: $p>0.05$, $^{**}p\leq0.01$, $^{***}p\leq0.001$ by
892 Mann-Whitney statistical test (b-g).
893
894

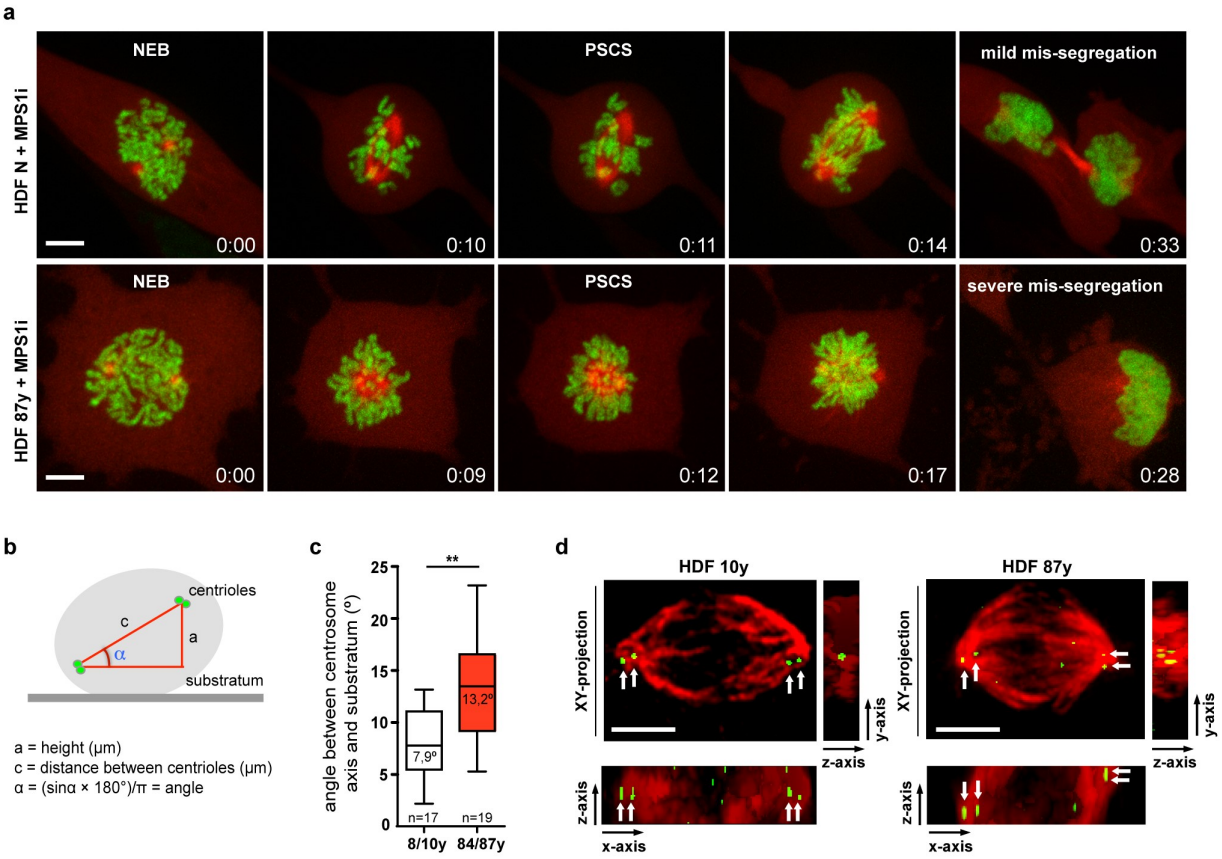

Macedo et al. Supplementary Figure 4

Supplementary Figure 4. Quantitative analysis of aging-associated mitotic defects. (a) Chromosome alignment delay. Representative movie frames of neonatal and elderly cells inhibited for Mps1 to prematurely exit mitosis in the presence of misaligned chromosomes. Examples of mild chromosome mis-segregation (bipolar anaphase without cytokinesis failure) (upper panel) and severe chromosome mis-segregation (failure in anaphase movement and cytokinesis) (lower panel) are shown. NEB, nuclear envelope breakdown. PSCS, precocious sister chromatid separation. Time min:sec. **(b-d)** Spindle mispositioning. **(b)** Scheme depicting the calculation of the spindle angle in relation to the growth surface. **(c)** Box-and-whisker plot with median, IQR and minimum and maximum values, illustrating the range of spindle angle values from young and elderly metaphase cells. n indicates sample size. $^{**}p \leq 0.01$ by

906 Mann-Whitney test. **(d)** Orthogonal projections (in xy, xz and yz axes) of the 3D distribution of
907 the spindle (α-tubulin, red) and centrioles (green) in young and elderly fibroblasts. Scale bar,
908 5 μm (a,d).
909
910

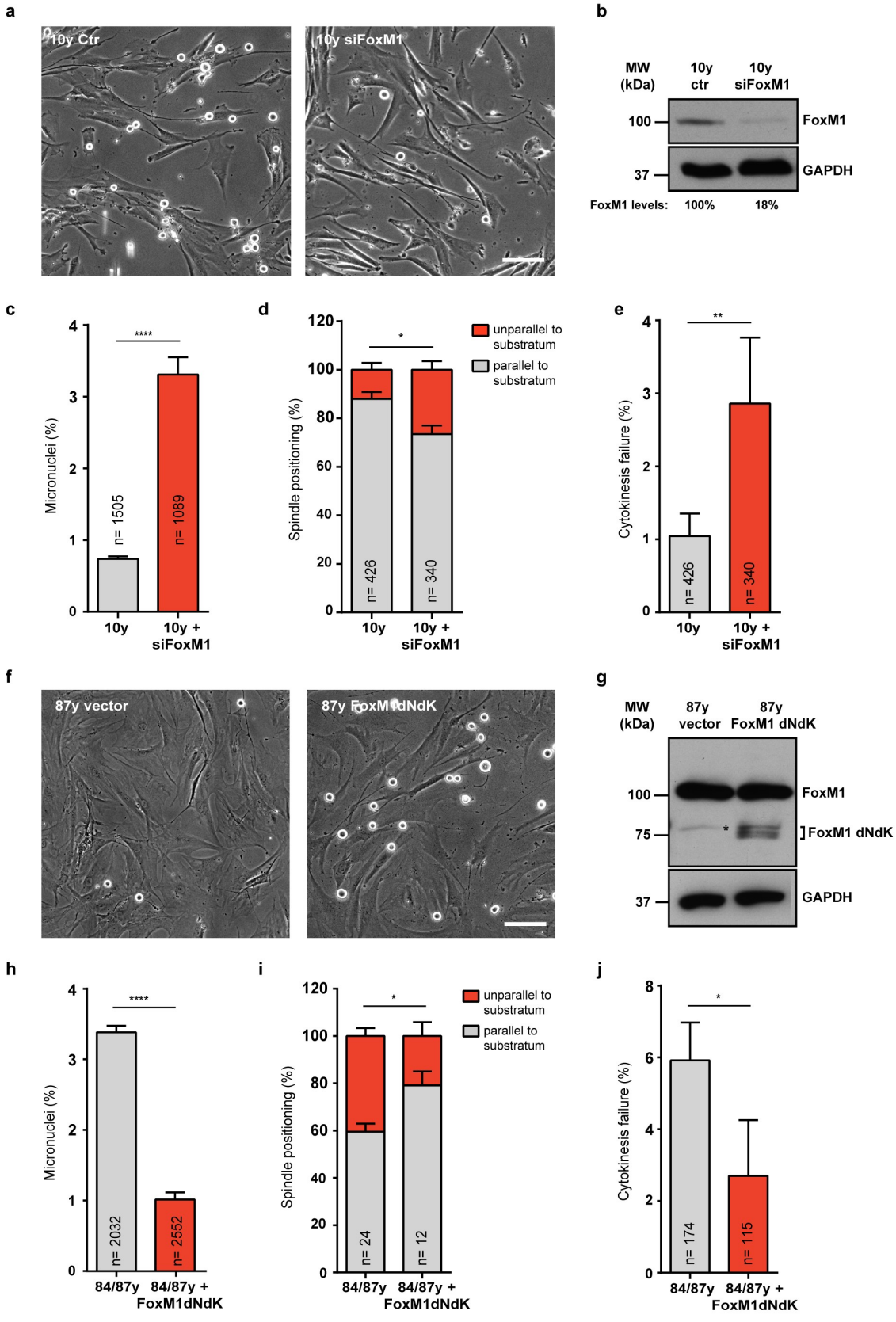

Macedo et al. Supplementary Figure 5

912 **Supplementary Figure 5. Modulation of FoxM1 levels affects mitotic fidelity. (a-e)** FoxM1
913 repression in young cells. **(a)** FoxM1 RNAi depletion (siFoxM1) decreases mitotic index. **(b)**
914 Western blot validation of FoxM1 decreased levels following RNAi. α-tubulin was used as
915 loading control. **(c)** Percentage of cells with micronuclei. **(d)** Percentage of mitotic cells
916 exhibiting unparalleled spindle to the substratum (in red). **(e)** Percentage of mitotic cells failing
917 cytokinesis. **(f-j)** Expression of constitutively active FoxM1 (FoxM1dNdK) in elderly cells. **(f)**
918 FoxM1dNdK expression increases mitotic index. **(g)** Western blot validation of FoxM1dNdK
919 expression. Asterisk indicates unspecific band in untransduced 87y cells. GAPDH was used as
920 loading control. **(h)** Percentage of cells with micronuclei. **(i)** Percentage of mitotic cells
921 exhibiting unparalleled spindle to the substratum (in red). **(j)** Percentage of mitotic cells failing
922 cytokinesis. Values are mean ± s.d. from three independent experiments. Sample size (n) is
923 indicated in each graph. *$p \leq 0.05$, **$p \leq 0.01$ and ****$p \leq 0.0001$ by two tailed $\chi 2$ statistical test.
924
925

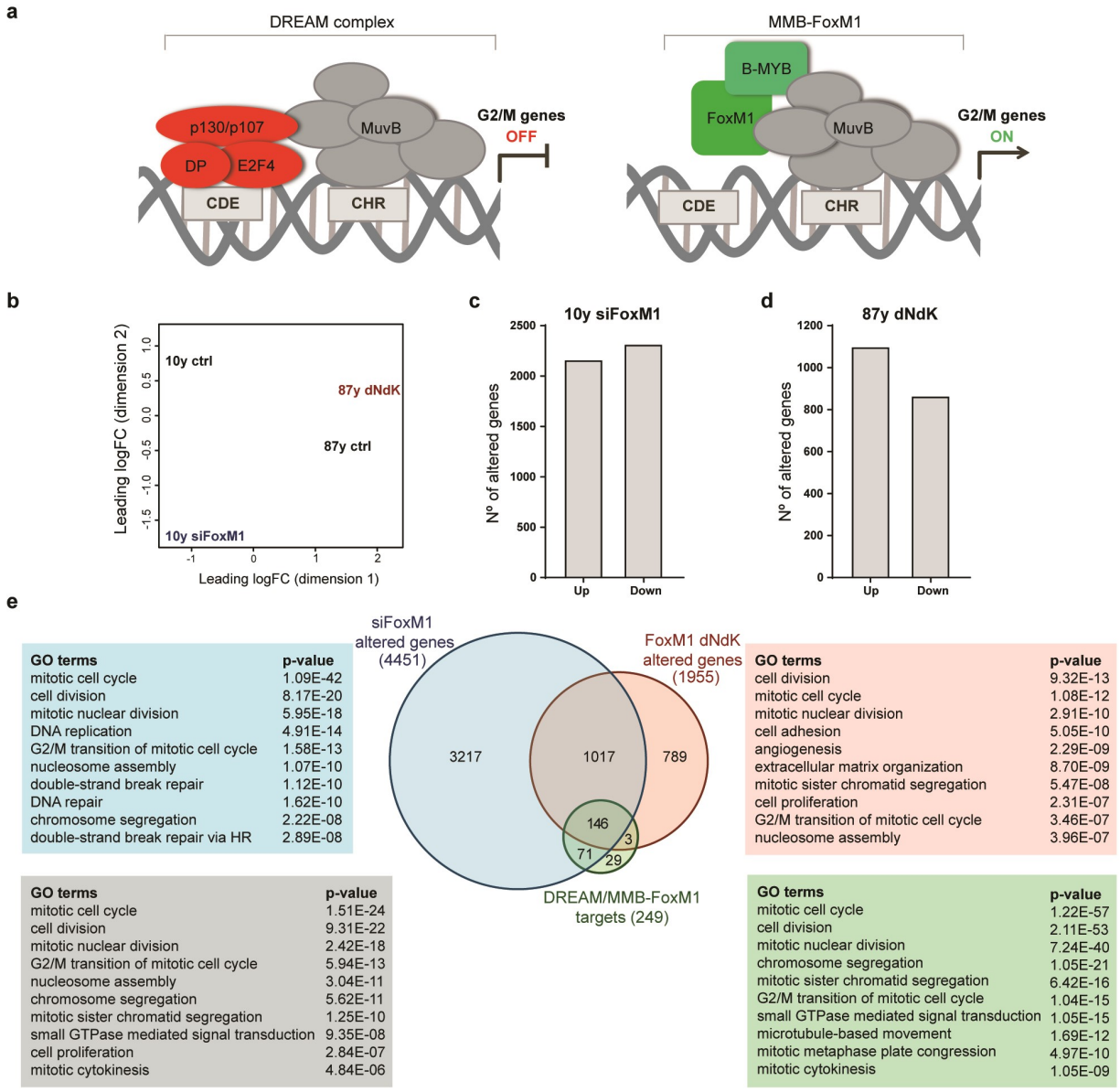

GO terms	p-value
mitotic cell cycle	1.09E-42
cell division	8.17E-20
mitotic nuclear division	5.95E-18
DNA replication	4.91E-14
G2/M transition of mitotic cell cycle	1.58E-13
nucleosome assembly	1.07E-10
double-strand break repair	1.12E-10
DNA repair	1.62E-10
chromosome segregation	2.22E-08
double-strand break repair via HR	2.89E-08

GO terms	p-value
cell division	9.32E-13
mitotic cell cycle	1.08E-12
mitotic nuclear division	2.91E-10
cell adhesion	5.05E-10
angiogenesis	2.29E-09
extracellular matrix organization	8.70E-09
mitotic sister chromatid segregation	5.47E-08
cell proliferation	2.31E-07
G2/M transition of mitotic cell cycle	3.46E-07
nucleosome assembly	3.96E-07

GO terms	p-value
mitotic cell cycle	1.51E-24
cell division	9.31E-22
mitotic nuclear division	2.42E-18
G2/M transition of mitotic cell cycle	5.94E-13
nucleosome assembly	3.04E-11
chromosome segregation	5.62E-11
mitotic sister chromatid segregation	1.25E-10
small GTPase mediated signal transduction	9.35E-08
cell proliferation	2.84E-07
mitotic cytokinesis	4.84E-06

GO terms	p-value
mitotic cell cycle	1.22E-57
cell division	2.11E-53
mitotic nuclear division	7.24E-40
chromosome segregation	1.05E-21
mitotic sister chromatid segregation	6.42E-16
G2/M transition of mitotic cell cycle	1.04E-15
small GTPase mediated signal transduction	1.05E-15
microtubule-based movement	1.69E-12
mitotic metaphase plate congression	4.97E-10
mitotic cytokinesis	1.05E-09

Macedo et al. Supplementary Figure 6

Supplementary Figure 6. Meta-analysis of differentially expressed genes upon modulation of FoxM1 levels. (a) Regulation of G2/M cell cycle genes through sequential binding of DREAM and MMB-FoxM1 to CHR promoter elements, as described in [38]. **(b)** Multidimensional scaling plot of distances between gene expression profiles based on sample RNA-sequencing. **(c)** Number of altered genes upon FoxM1 RNAi in 10y cells. **(d)** Number of altered genes upon lentiviral transduction of 87y cells with FoxM1dNdK. Genes are listed in Supplementary Table

1. **(e)** Venn diagram displaying the overlaps between siFoxM1 altered genes, FoxM1dNdK altered genes and targets of both DREAM and MMB-FoxM1 complexes [43] (Supplementary Table 2). The respective top ten GO terms are organized by *p*-values using the DAVID Functional Annotation tool.

Supplementary Table 1. RNA-sequencing data sets. Table includes comparative gene expression analysis.

Supplementary Table 2. Venn Diagram data sets. Overlap between FoxM1 RNAi altered genes, FoxM1dNdK altered genes, and DREAM/MMB-FoxM1 targets. Table includes all the overlapping clusters represented in the Venn diagram. Genes are listed accordingly to Ensembl ID.

Supplementary Table 3. Primers used in qPCR and cloning.

Supplementary Video 1. From left to right. Mitotic progression of a neonatal fibroblast (HDF N) co-expressing H2B-GFP (green) and α-tubulin-mCherry (red). Chromosome congression delay in a dividing elderly fibroblast (HDF 87y) co-expressing H2B-GFP (green) and α-tubulin-mCherry (red). Chromosome anaphase lagging and micronucleus formation in a dividing elderly fibroblast (HDF 87y) co-expressing H2B-GFP (green) and α-tubulin-mCherry (red). Unparalleled mitotic spindle positioning in relation to the growth surface and asynchronous adherence of the daughter cells in a dividing elderly fibroblast (HDF 87y) co-expressing H2B-GFP (green) and α-tubulin-mCherry (red). Time-lapse images were acquired on a spinning-disk

confocal microscope using 90 s intervals. Time min:sec. Frame series from this movie were used in Fig. 2a-d.

Supplementary Video 2. From left to right. Mitotic delay from nuclear envelope breakdown (NEB) to anaphase onset (ANA) in an elderly fibroblast (HDF 87y) co-expressing H2B-GFP (green) and α-tubulin-mCherry (red). Mitotic efficiency rescue following expression of FoxM1dNdK in an elderly fibroblast (HDF 87y) co-expressing H2B-GFP (green), α-tubulin-mCherry (red). Time-lapse images were acquired on a spinning-disk confocal microscope using 90 s intervals. Time min:sec. Frame series from this movie were used in Fig. 5b.

Supplementary Video 3. From left to right. Chromosome alignment delay and mitotic spindle mispositioning in a HGPS (Progeria) fibroblast co-expressing H2B-GFP (green) and α-tubulin-mCherry (red). Mitotic efficiency rescue following FoxM1dNdK expression in a HGPS (Progeria) fibroblast co-expressing H2B-GFP (green) and α-tubulin-mCherry (red). Time-lapse images were acquired on a spinning-disk confocal microscope using 90 s intervals. Time min:sec. Frame series from this movie were used in Fig. 5i.